UNIVERSIDADE
BEIRA INTERIOR

Development of a Propeller Blade for a Variable Pitch Mechanism

(Versão corrigida após defesa)

André Filipe Gomes Rodrigues

Dissertação para obtenção do Grau de Mestre em
Engenharia Aeronáutica
(mestrado integrado)

Orientador: Prof. Doutor Miguel Ângelo Rodrigues Silvestre

março de 2022

Acknowledgments

I would like to thank Professor Miguel Silvestre for bringing this subject to me, sharing his knowledge and increasing my interest about the theme.

To Pedro Alves, for helping me in propellers printing process and wind tunnel tests.

To my parents for supporting me on this academic journey.

Resumo

Tendo em conta o aumento do número de aeronaves de descolagem e aterragem vertical que seguem a crescente evolução do conceito de mobilidade aérea urbana, é importante utilizar uma hélice adequada para as características dessas aeronaves. O objetivo deste trabalho passou pelo desenvolvimento da pá de uma hélice que apresentasse o melhor desempenho propulsivo possível quando utilizada num mecanismo de passo variável. Desta forma, foi obtida a geometria da pá de uma hélice admissível para ser utilizada em diferentes fases de voo, tanto na descolagem ou no voo pairado onde se torna benéfico utilizar a hélice com passo fino, como em voo de cruzeiro onde utilizar um passo grosso é mais adequado. Após ser encontrada a geometria da hélice que assegurava os objetivos pretendidos, a mesma foi impressa utilizando uma impressora 3D de modelagem por deposição fundida e posteriormente analisada no túnel de vento. Diversas técnicas foram aplicadas tanto no modelo do desenho assistido por computador, como das definições de impressão da impressora e mesmo no processo de acabamento das hélices afim de obter os resultados mais rigorosos possíveis. Sendo assim, os resultados numéricos foram comparados com os resultados obtidos no túnel de vento, apresentando pequenas diferenças, que por se manterem consistentes com outras hélices analisadas sobre as mesmas condições, permitem considerar a impressão 3D como uma opção de baixo custo para obter um protótipo de uma hélice que possa ser submetida a testes de desempenho experimentais.

Palavras-chave

Hélice de passo variável, modelo de hélice em desenho assistido por computador, impressão de hélice em 3D

Abstract

Considering the evolution of the urban air mobility concept and the increasing number of vertical takeoff and landing aircraft in development, the use of the correct propeller for this kind of aircraft is paramount. This dissertation's purpose is to develop a propeller blade with a propulsive efficiency as good as possible when used in a variable pitch mechanism. A blade propeller geometry was developed to be used in the different stages of flight. Therefore, during take-off, climbing and hover conditions the propeller can be used with low pitch to increase the performance in thrust per unit power. On the other hand, during cruise flight condition the propeller can be used with a coarse pitch to operate with greater propulsive efficiency. A proper propeller blade geometry was achieved. The respective CAD model with additional features was developed to build a prototype of the propeller using a FDM 3D printer. Specific printing settings and different finishing processes were applied to obtain the most accurate results possible. Comparing numerical and experimental results small divergences were realized. Considering the similarity between the results and the similar divergences that also occurred in the analysis of different propellers tested in identical conditions are indicators that it is possible to use 3D printing as a low cost way of rapid prototyping low Reynolds number propellers geometries that can be submitted to experimental performance tests.

Keywords

Variable pitch propeller, Propeller CAD model design, 3D printed propeller

Contents

List of Figures

List of Tables

List of Acronyms

3D	Three-Dimensional
ABS	Acrylonitrile Butadiene Styrene
BEM	Blade Element Momentum
CAD	Computer-Aided Design
CNC	Computerized Numerical Control
eVTOL	electric Vertical Takeoff and Landing
FDM	Fused Deposition Modelling
LOM	Laminated Object Manufacturing
MIL	Minimum Induced Loss
MJM	Multi-Jet/Polyjet Modelling
MTP	Maximum Total Power
NACA	National Advisory Committee for Aeronautics
PET-G	Polyethylene Terephthalate Glycol
PLA	Polylactic Acid
SLA	Stereo Lithography
SLS	Selective Laser Sintering
UAV	Unmanned Aerial Vehicles
UBI	University of Beira Interior
VTOL	Vertical Takeoff and Landing

List of Symbols

Symbol	Description	Units
A	Propeller disk area	[m^2]
a_a	Axial induction factor	[-]
a_t	Radial induction factor	[-]
B	Number of blades	[-]
c	Blade chord length	[m]
C_l	Lift coefficient	[-]
C_d	Drag coefficient	[-]
C_p	Power coefficient	[-]
C_t	Thrust coefficient	[-]
D	Propeller diameter	[m]
E	Prandlt correction factor	[-]
E_{tip}	Blade tip Prandlt correction factor	[-]
E_{root}	Blade root Prandlt correction factor	[-]
F_a	Axial force	[N]
F_t	Tangential force	[N]
J	Advance ratio	[-]
n	Rotation speed	[rev/s]
P	Power	[W]
p_0	Pressure far upstream and downstream propeller disk	[Pa]
p_1	Pressure downstream propeller disk	[Pa]
p_2	Pressure upstream propeller disk	[Pa]
Q	Torque	[Nm]
R	Maximum propeller radius	[m]
T	Thrust	[N]
V_0	Freestream velocity	[m/s]
V_a	Induced axial velocity	[m/s]
V_d	Propeller disk air velocity	[m/s]

Symbol	Description	Units
V_s	Upstream velocity	$[m/s]$
V_t	Induced tangential velocity	$[m/s]$
W	Relative flow velocity	$[m/s]$
W_a	Axial velocity	$[m/s]$
W_t	Tangential velocity	$[m/s]$
x_{ca}	Center of area abscissa	[-]
x_{te}	Trailing edge abscissa	[-]
y_{ca}	Center of area ordinate	[-]
y_{te}	Trailing edge ordinate	[-]

Greek Alphabet Letters

Symbol	Description	Units
α	Angle of attack	[º]
Δp	Pressure difference	[Pa]
$\Delta\beta$	Pitch incidence angle variation	[º]
η	Efficiency	[-]
Ω	Rotor velocity	[rad/s]
ϕ	Inflow angle	[º]
ρ	Air density	[kg/m^3]
θ	Incidence angle	[º]

Chapter 1

Introduction

1.1 Motivation

Since forever, the human being develops mechanisms to facilitate daily activities and improve its comfort. But in the last years these developments and daily activities need to concern with the sustainability and preservation of our planet. Greenhouse gases are the principal cause of global warming and a considerable part of these gases come directly or indirectly from the transportation mobility adopted by the population. At the same time, earth population does not stop to increase and the adjustment of this growth with a convenient and sustainable system concerning human mobility is expected. Furthermore, traffic congestion as a consequence of population growth has a massive impact on air pollution [1].

Urban air mobility appears as a new concept of mobility to face the necessity of overtaking the road traffic congestion and reducing greenhouse gases emissions. A specific kind of aerial vehicle, the electric Vertical Takeoff and Landing (eVTOL) aircraft is adjusted to this concept [2]. Considering the diversity of eVTOL vehicles already existing, for the case of propeller propulsion system there are still some differences in the concepts used to get thrust in the different stages of the flight.

eVTOL can be classified as Vectored Thrust (see Figure 1.1) when the aircraft uses the same propulsion system for take-off and cruise flight. These aircraft have a wing and the propulsion system tilts into a near vertical thrust line for hover, take-off and landing, tilting back the thrust line to an horizontal direction when the aircraft transitions to cruise flight. Lift+cruise eVTOL (see Figure 1.2) have two different propulsion systems, one for vertical flight or hover and the other one for the cruise flight.

Figure 1.1: Representation of a passenger Vectored Thrust Vtol concept in hover (top) and flight (bottom) from [3]

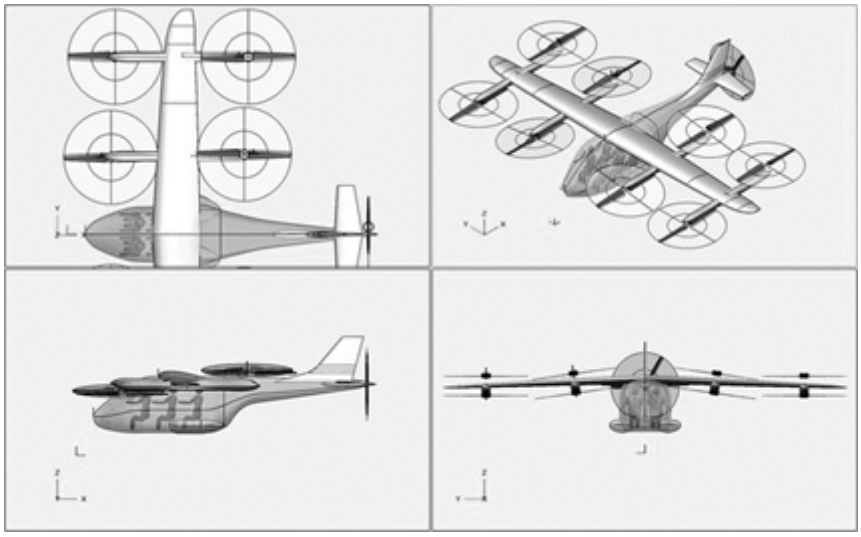

Figure 1.2: Representation of a Lift+Cruise Vtol aircraft from [4]

The eVTOL can also be wingless, usually having multiple rotors and being efficient for take-off and hover but not suitable for long distance operations. Additionally, there are the eHelos that work as electric helicopters [5].

Lift+cruise eVTOL aircraft are usually manufactured with fixed pitch propellers. The propellers optimized for the vertical flight do not present great propulsive efficiency during cruise flight and for that reason another propulsion system is working during that flight condition using coarse pitch propellers. The problem of this concept design is that during the flight there are propellers that are not producing thrust and the drag created is negatively

affecting aircraft endurance.

In the case of Vectored Thrust eVTOL aircraft applying a variable pitch mechanism could bring several advantages. The possibility of modifying the propeller pitch is the principle that allows increasing propeller performance. For example, during the most efficient cruise flight condition, when minimum thrust is required, propeller propulsive efficiency is greater for coarse pitch. On the other hand, low pitch increase the performance in thrust per unit power of the propeller for take-off, climbing and hover conditions when the propulsive system needs to provide larger thrust magnitudes.

The issue with a propeller developed for a variable pitch mechanism is that it can only be optimized for a certain pitch, usually the pitch to be used in cruise flight condition. The goal of this work is to develop a blade geometry with propulsive efficiency as good as possible in the full range of pitch values it will operate in.

1.2 Contribution

There are two main purposes with this dissertation:

1. To study different concepts applied in the design process of a blade propeller and at the same time analyze which one generates propellers with better performance in variable pitch operational conditions.

2. To introduce different strategies to effectively manufacture a propeller prototype using a Fused Deposition Modelling 3D printer. This allows to speed up the validation of a new propeller design. The development of the CAD model, insertion of additional features, printing settings and finishing process are presented to provide a low cost way of prototyping small UAVs, including eVTOL propellers that can be submitted to experimental performance tests. These experimental tests can work as a complement to the already existing propellers design and analysis programs.

1.3 Structure

This dissertation is divided into five chapters.

The first chapter presents the problems associated with the general mobility concept existing mainly in the big cities and presents an alternative, the urban air mobility with the use of eVTOLs. The objectives of this work are presented, as well as the dissertation guidelines.

In the second chapter a literature review is presented. Fundamental principles related with propellers that are the basis of most codes used to analyze and develop new propeller geometries are presented. A state of the art is also included with a review of the relevant works that focus on the design of propellers, as well as the works that point to the development of propellers using FDM 3D printing.

In chapter three the methodology of the present work is described. Firstly, different steps to measure the geometry of an existing propeller that can be later numerically analyzed are presented. Then, different concepts to achieve a propeller blade geometry with satisfactory performance in variable pitch operational conditions are presented. The way that desirable propeller geometries are reproduced in a CAD model and different approaches to print the propellers are described. Finally, the experimental setup to test 3D printed propellers in the wind tunnel is reported.

In chapter four the obtained results are presented and discussed. Based on several numerical results corresponding to the propellers designed for different variable pitch propeller concepts, two propellers were chosen to be 3D printed and tested in the wind tunnel. Wind tunnel results and numerical results are compared and the reason why both propellers were 3D printed is explained.

In the final chapter, the conclusions from the whole work are exposed along with some work that can be done in the future related with this dissertation.

Chapter 2

Literature Review

2.1 Fundamental Theory

2.1.1 Momentum theory

The momentum theory, also designated as actuator disk theory, was first presented by Froude [6] as the continuation of Rankine work [7]. In this theory the propeller is considered as a disk and its flow forms a stream tube characterized by an acceleration when passing through the disk. In this theory, compressibility, viscous and rotational effects in the flow are not considered. The flow is considered purely axial.

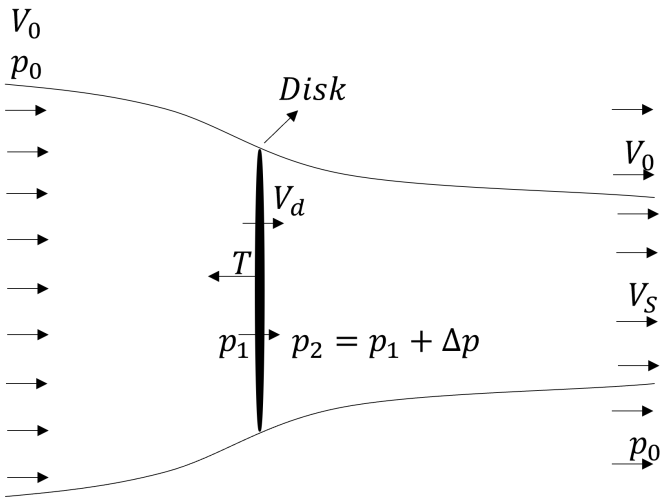

Figure 2.1: Propeller momentum theory stream-tube

As the mass flow rate remains constant in the stream tube, the thrust produced by the propeller can be calculated.

$$T = A\rho V_d \left(V_S - V_0\right) \quad (2.1)$$

Where A is the propeller disk area, V_d the propeller disk air velocity, V_0 the freestream velocity and V_S the upstream velocity.

The pressure far upstream and downstream is p_0. However, near the actuator disk the pressure suddenly drops upstream the disk and immediately rises downstream next to the disk.

Considering the upstream and downstream velocities and that the thrust is related with the pressure change across the propeller disk, using Bernoulli's equation:

$$T = A\Delta p \quad (2.2)$$

$$\Delta p = [p_0 + \frac{1}{2}\rho V_S^2] - [p_0 + \frac{1}{2}\rho V_0^2] \quad (2.3)$$

$$\Delta p = \frac{1}{2}\rho(V_S^2 - V_0^2) \quad (2.4)$$

$$T = \frac{1}{2}A\rho(V_S^2 - V_0^2) \quad (2.5)$$

Combining Equations 2.1 and 2.5 for the propeller disk velocity:

$$V_d = \frac{1}{2}(V_S + V_0) \quad (2.6)$$

So, according to Equation 2.6 the velocity of the air passing through the propeller disk is the average between the far upstream and downstream velocities.

2.1.2 Blade Element Theory

The momentum theory presented in 2.1.1 concerns the air flow through the stream tube created by the propeller action. On the other hand blade element theory [8] considers the geometry of the blade. The blade is divided in small elements along its span, considered independent of each other and can be analyzed aerodynamically as two-dimensional airfoil sections with respective chord and incidence angle. At each element, the produced thrust and torque are calculated.

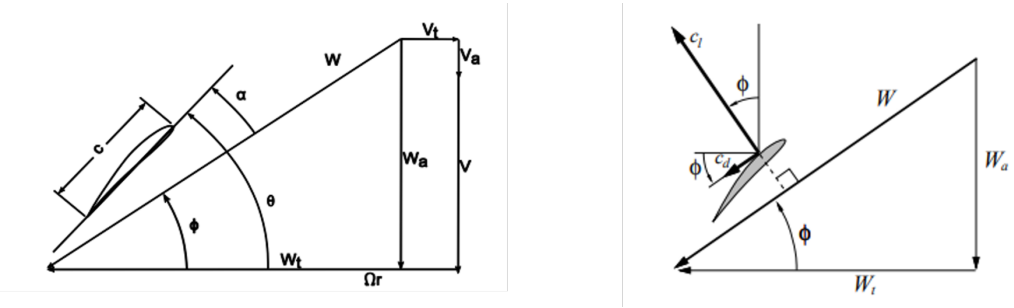

Figure 2.2: Blade element geometry and respective local lift and drag coefficients [9]

Lift and drag forces are proportional to lift and drag coefficients and can be calculated by Equations 2.7 and 2.8.

$$dL = \frac{1}{2}\rho W^2 C_L c dr \quad (2.7)$$

$$dD = \frac{1}{2}\rho W^2 C_D c dr \quad (2.8)$$

W^2 represents the local blade element's relative flow speed.

Using values of lift and drag, differential thrust and torque are calculated by

$$dT = dL\cos\phi - \ dD\sin\phi \quad (2.9)$$

$$dQ = r\ dT \quad (2.10)$$

$$dT = \frac{1}{2}\rho W^2 (C_L\cos\phi - C_D\sin\phi) c dr \quad (2.11)$$

$$dQ = \frac{1}{2}\rho W^2 (C_L\sin\phi - C_D\cos\phi) c r dr \quad (2.12)$$

This methodology only presents differential thrust and torque in each considered element position along the blade radius. To calculate total thrust and torque of propeller, an integration across the blade radius must be done and the value multiplied by the number of blades,

B, according to Equations 2.13 and 2.14.

$$T = B \int_0^r \frac{1}{2} \rho W^2 (C_L \cos\Phi - C_D \sin\Phi) c dr \quad (2.13)$$

$$Q = B \int_0^r \frac{1}{2} \rho W^2 (C_L \sin\Phi - C_D \cos\Phi) c r dr \quad (2.14)$$

2.1.3 Blade Element Momentum Theory

The Blade Element Momentum(BEM) Theory presented by Glauert in [10] comes up as a conjugation of the two previous theories. Induced velocities components are determined from the momentum theory. The blade is also divided in small elements along the span and define their own annulus when they rotate while momentum balance occurs across the rotor plane (see Figure 2.3).

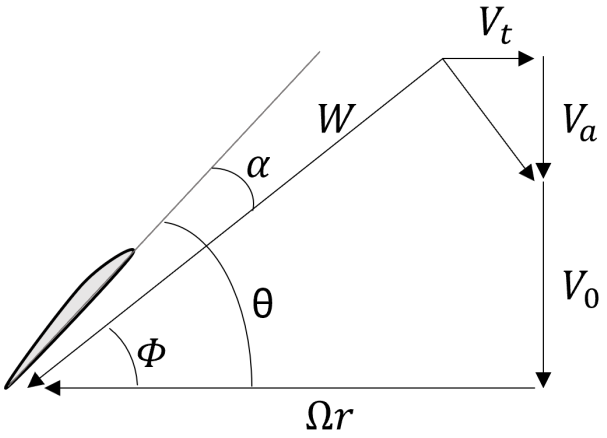

Figure 2.3: Velocities and angles decomposition at radial location r

The axial velocity W_a is the sum of freestream airspeed V_0 with induced axial velocity V_a and tangential velocity W_t that is the sum of velocity related with propeller rotation Ωr with the induced tangential velocity, V_t. The angle of attack α is defined as the difference between incidence angle θ and inflow angle ϕ and is used to determine lift and drag coefficients. The inflow angle that is the angle of the relative flow to the blade element with respect to the rotor plane is calculated from the axial and tangential induced velocities and local speed according

to Equation(2.15).

$$\tan \Phi = \frac{V_0 + V_a}{\Omega \, \mathrm{r} - V_t} = \frac{V_0 \, (1 + a_a)}{\Omega \, \mathrm{r} \, (1 - a_t)} \quad (2.15)$$

The axial induction factor is defined as

$$a_a = \frac{V_a}{V} \quad (2.16)$$

The tangential induction factor is defined as

$$a_t = \frac{V_t}{\Omega \, \mathrm{r}} \quad (2.17)$$

The axial and tangential force coefficients are obtained from:

$$C_a = C_L \cos \Phi - C_D \sin \Phi \quad (2.18)$$

$$C_t = C_L \sin \Phi + C_D \cos \Phi \quad (2.19)$$

The axial and tangential forces are obtained from the force coefficients according to:

$$F_a = \frac{1}{2} \rho W^2 c C_a \quad (2.20)$$

$$F_t = \frac{1}{2} \rho W^2 c C_t \quad (2.21)$$

The thrust and torque contribution of each blade element is:

$$dT = F_a dr \quad (2.22)$$

$$dQ = r F_t dr \quad (2.23)$$

And finally, total thrust and torque of the propeller can be calculated from:

$$T = B \sum_{i=1}^{n} F_{a_i} \quad (2.24)$$

$$Q = B \sum_{i=1}^{n} F_{t_i} r \quad (2.25)$$

2.1.4 Prandtl Tip and Hub losses

In the BEM theory, the calculated two-dimensional forces do not consider the influence of tip and hub vortices in the induced velocities near these propeller blade regions. Therefore, Prandtl presents a correction factor (Equation 2.26) [11] that accounts for the influence of each blade element proximity to the blade tip or hub regions to correct its capacity to generate lift.

$$E = \frac{2}{\pi} \cos^{-1}\left(e^{-f}\right) \quad (2.26)$$

$$f_{tip} = \frac{B}{2} \frac{R - r}{r \sin \Phi} \quad (2.27)$$

$$f_{hub} = \frac{B}{2} \frac{r - R_{hub}}{r \sin \Phi} \quad (2.28)$$

When both tip and hub losses are considered, the total correction factor is

$$E = E_{tip} E_{root} \quad (2.29)$$

This correction factor is used to modify the induction factors from Blade Element Momentum Theory (Equations 2.30 and 2.31).

$$a_a = \left(\frac{4E \sin^2 \Phi}{\frac{cB}{2\pi r} C_a} - 1 \right)^{-1} \quad (2.30)$$

$$a_t = \left(\frac{4E \sin\Phi \cos\Phi}{\frac{cB}{2\pi\, r} C_t} + 1 \right)^{-1} \quad (2.31)$$

2.1.5 Propeller Performance Parameters

The propeller performance parameters are dimensionless coefficients used to describe, analyze and compare different propellers. In propeller literature, different coefficients definitions can be found to compare the propellers. The ones presented here, follow the most standard definition based on NACA publications. The advance ratio is defined (Equation 2.32) as the ratio of forward velocity and the product of rotational speed in revolutions per second and diameter. In practice, it is proportional to the angle between the relative wind to the blade tip element and the rotor plane.

$$J = \frac{V}{nD} \quad (2.32)$$

The thrust coefficient (C_t) (Equation 2.33), power coefficient (C_p) (Equation 2.34) and propulsive efficiency (η) (Equation 2.35) are used to analyze performance aspects of the propeller for different values of advance ratio.

$$C_t = \frac{T}{\rho\, n^2 D^4} \quad (2.33)$$

$$C_p = \frac{P}{\rho\, n^3 D^5} \quad (2.34)$$

$$\eta = \frac{C_t}{C_p}\, J \quad (2.35)$$

where *P* corresponds to shaft power that can be calculated as:

$$P = \Omega\, \mathrm{Q} \quad (2.36)$$

2.2 State of art

2.2.1 Design of optimum propellers

The modern design of propellers can be traced back to 1979 when a propeller design method, based on Betz's condition [12] for minimum induced loss, was presented by Larrabee [13]. A series of propeller blade design equations were implemented to achieve the geometry of a quiet and efficient propeller. Later in 1994, Adkins and Liebeck [14] based on Larrabee work applied correction factors to get the design methods completely according with the propeller analysis. Since then, these methods were used to feed different code improvements and other models emerged to further improve optimum propeller design.

QPROP [15] and QMIL [16] are both propeller study programs that were used in this project. Developed by Mark Drela, QPROP is an analysis program that predicts performance of propeller motor combinations and QMIL is a design program capable to generate propeller geometries for Minimum Induced Loss (MIL), or windmill geometries for Minimum Induced Loss or Maximum Total Power (MTP). Both are based in an extension of blade element/vortex formulation. A detailed and complete description of the theoretical formulation can be seen in [9].

2.2.2 Propeller FDM 3D printing

3D printing is an additive manufacturing process where a product can be developed from a CAD model and then a printer can produce the three-dimensional object layer by layer [17]. It appears as an alternative propeller manufacturing technique that offers the researchers an accessible way to analyze a propeller performance in an early stage of propeller design iteration where small changes in the product design can be made to the CAD model followed by the immediate printing of the 3D object.

3D printing can be divided in different types, essentially depending on the technology used to print the layers, the most popular being Fused Deposition Modelling (FDM), Laminated Object Manufacturing (LOM), Multi-Jet/PolyjetModelling (MJM), Selective Laser Sintering (SLS) and Stereo Lithography (SLA) [18].

FDM is an additive manufacturing method where a thermoplastic filament is melted under

specific conditions to be extruded creating an object where the stacking layers are fused together. The portable FDM 3D printer can be easily acquired, showing itself as one of the most low-cost type of 3D printing technology. Reference [19] compares different filaments used in FDM technologies.

There are different filaments that can be used in a FDM 3D printer and the choice for the material must consider the desired mechanical properties for the printed product, its dimensions and shape. Some of the most used filaments are Polylactic acid (PLA), Polyethylene terephthalate glycol (PET-G) and Acrylonitrile butadiene styrene (ABS). PLA is the cheapest and strongest material compared with the other two and that is the reason why it is the most used filament, being only passed over for situations where it is required a material with greater tolerance to temperature and in that case ABS filament is more suitable.

2.2.3 3D printed propellers performance and mechanical properties

The usual process of propeller manufacturing involves injection molding or CNC machining. Being a non-conventional way to manufacture propellers, different studies were made to evaluate the performance of 3D printed propellers compared with more conventional manufacturing techniques. In [20] researchers compared an injection molded propeller with different 3D printed PLA propellers manufactured with specific printing settings, varying nozzle extruder temperature, printing speed and layer height. According to the results, thrust reading of different 3D propellers seems to resemble the values of the original injection molded propeller from 2400 rpm to 7500 rpm. Torque readings of 3D printed propellers are generally higher than the original propeller and consequently the power consumption. However, for some specific printing settings the researchers conclude that both thrust and torque readings of the different 3D printed propellers present similar values to the injection molded propeller and for that reason 3D printing can be used as an effective type of manufacturing propellers to approximate the performance with an injection molded propeller.

In [21] researchers use ABS to manufacture different propellers, varying infill percentage and testing the thrust produced for each one. Increasing propeller infill suggests an increase in the thrust produced for the propeller with small changes in its mass. In this study, researchers only achieved a 78% thrust compared with injection molded propeller.

In [20] researchers evaluated the mechanical properties of 3D manufactured propellers using a Charpy impact testing machine and concluded that the impact strength of FDM propellers is lower than an injection molded propeller. Modifying printer settings (extruder temperature, printing speed, and layer height) can have consequences in the mechanical properties of the printed material. The use of higher tensile strength material such as carbon fiber composite can improve the strength of the propeller [22].

Chapter 3

Methodology

In this chapter the concepts behind the development of a blade geometry to be used in a variable pitch mechanism are described as well as the CAD blade model design to manufacture the respective blade. Firstly, an Aeronaut Camcarbon 15x8 folding blades propeller was submitted to a geometry measurement and analysis in QPROP to be used as a reference. Then, different concepts for the development and optimization of a blade propeller to be used in a variable pitch mechanism are presented. A specific blade propeller design is chosen to be replicated in a CAD model and printed in a FDM 3D printer. Finally, the finishing processes applied to the manufactured propeller before it can be tested in the wind tunnel are presented.

3.1 Aeronaut Camcarbon 15x8 Propeller Study

An Aeronaut Camcarbon 15x8, that was the reference propeller in the development of an eVTOL in University of Beira Interior was analyzed in QPROP to use its performance as benchmark against a propeller developed specifically for eVTOL variable pitch operational conditions. To be possible to analyze the performance of the Aeronaut Camcarbon propeller, it was necessary to present a description of the blade geometry, including the blade airfoils.

3.1.1 Camcarbon 15x8 geometry measurement

Following a similar measurement procedure as presented by Mark Drela [23] and making adjustments for the available tools, a series of steps were applied to obtain the blade geometry.

1. Parallel lines were drawn in a rectangular board with 1cm spacing.

2. Using hot glue, two identical drill bits and another cylindrical metal rod with the same radius as the root hub support hole of propeller hub, the blade was attached to the

board totally supported with the same incidence as it would have relative to the original propeller hub and with the attachment hole axis parallel to the board drawn lines, making sure that the tip of the blade was tangent to one of the lines drawn on the board (see Figure 3.1).

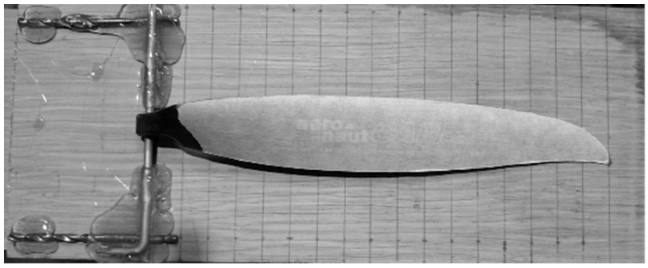

Figure 3.1: Aeronaut Camcarbon 15x8 blade fixed to a rectangular board with 1cm spacing parallel lines

3. Starting from the tip and using a folding material the different sections were marked in the blade previously covered with masking tape (Figure 3.2).

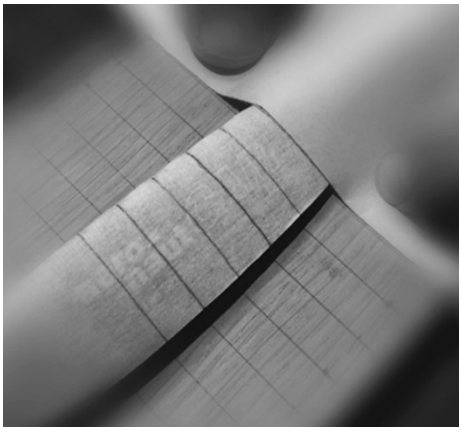

Figure 3.2: Illustrative moment of a folding material being used to mark different sections of the blade covered with masking tape.

4. After being cut close to the trailing edge (to enable the measure of larger angles near the rotational axis) the board was placed on two supports and to make sure it was over a horizontal plane a level was used.

5. An angle ruler was used to facilitate the incidence angles measuring process. Two metal cutting saws were added to both sides of the angle ruler to work as extensions and six small magnets held two nails parallel to this reference direction (three magnets for each nail) (see Figure 3.3).

6. The process to measure the angle was the same for all sections. Firstly, lower the arm of the angler ruler was positioned under the board touching it to remain parallel to its surface and the other arm was adjusted until one nail was pointing to the leading edge of the section being measured while the other nail was pointing to the respective trailing edge (see Figure 3.3).

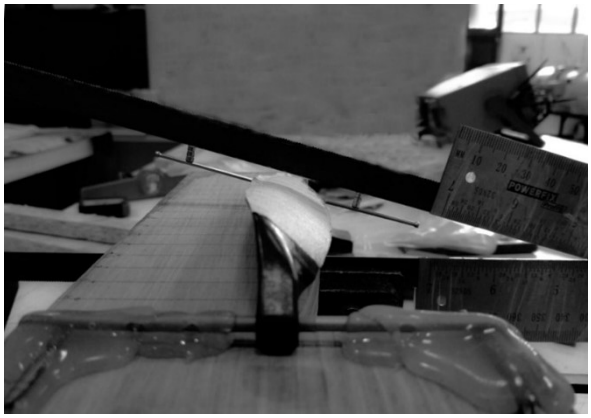

Figure 3.3: Measurement of the incidence angle of the blade in the respective section.

7. Since it is a procedure that is subjected to some uncertainty over the read value, an exponential trend line (see Equation 3.1) was obtained with the read values of incidence angles to filter out random variance and thus achieve more accurate results.

$$\theta_{tl} = 1558.1 r^{-0.96} \quad (3.1)$$

Where θ_{tl} is the incidence angle of the trend line in the section with radius r

8. After the incidence angles of all sections were measured, the blade was released from the board and the chord in different sections was measured using a digital caliper. The values of chord and incidence angle in each section can be seen in Table 3.1.

Radius (mm)	Chord 1st measure (mm)	Chord 2nd measure (mm)	Chord 3rd measure (mm)	Chord mean value (mm)	Incidence angle (°)	Incidence angle from the trend line (°)
40.5	21.31	21.3	21.38	21.33	42	44.61
50.5	23.79	23.79	23.82	23.80	36	36.09
60.5	25.4	25.55	25.5	25.48	30.3	30.35
70.5	26.48	26.49	26.48	26.48	27.2	26.20
80.5	26.97	26.94	26.94	26.95	24.7	23.07
90.5	27.04	27.02	26.96	27.01	22.4	20.62
100.5	26.8	26.92	26.8	26.84	18	18.64
110.5	26.31	26.39	26.38	26.36	16.5	17.02
120.5	25.3	25.26	25.25	25.27	15.2	15.66
130.5	23.92	23.85	23.88	23.88	14.9	14.51
140.5	21.98	22.02	21.95	21.98	13	13.52
150.5	19.98	20.02	20	20.00	12.1	12.65
160.5	17.34	17.58	17.45	17.46	11.9	11.89
170.5	14.45	14.49	14.49	14.48	11.5	11.22
180.5	10.96	10.91	10.83	10.90	11.2	10.63
190.5	0.84	0.91	0.86	0.87	9.6	10.09

Table 3.1: Chord and incidence angles in different sections of Aeronaut Camcarbon 15x8 blade

9. According to [23] the 75% radius blade section was carefully wrapped with a solder wire to replicate the airfoil in that position and then it was carefully removed from the blade to present a clear image of the airfoil shape.

10. A picture of the respective airfoil was taken and edited to draw a perpendicular line to the chord of the airfoil with the same length (see Figure 3.4).

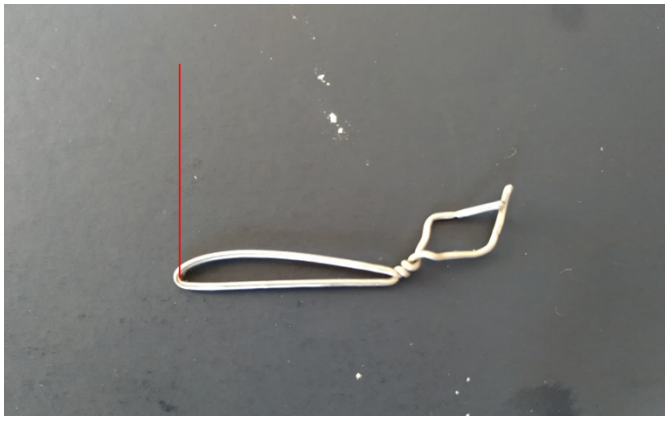

Figure 3.4: Airfoil picture of Aeronaut Camcarbon 15x8 blade at 0.75 radius edited with a perpendicular line to the chord with the same length

11. Web Plot Digitizer [24] was used to turn the airfoil shape into coordinates data. Both X and Y axis were defined in this program. X axis crosses the chord of the airfoil, where point 0 corresponds to leading edge point and point 1 to trailing edge point. Point 0 of

the Y axis corresponds to the leading edge point and point 1 to the end of a perpendicular line to the chord with the same length previously drawn in the picture. Numerical data was exported and the airfoil could be analyzed.

3.1.2 Camcarbon 15x8 QPROP analysis

QPROP [15] is an analysis program that predicts the performance of propeller-motor combinations. Two input files are required to run the program, one of them with the description of the blade and the other describing the motor being used. As the objective of the work includes studying the propellers blades performance, the same motor input file which was provided in the download program runs folder was used for every QPROP analysis . In the file the motor characteristics are specified (Figure 3.5).

```
Axi 4130/20

 1

 0.099    ! Rmotor (Ohms)
 1.60     ! Io     (Amps)
 305.0    ! Kv     (rpm/Volt)
```

Figure 3.5: Motor input file for QPROP

Propeller input file is more complex, with a detailed description of the blade (see Figure 3.6). Line 1 specifies the number of blades and propeller radius. The values that characterize airfoil at 0.75 blade radius are inserted from lines 2 to 5 and will be explained later. Line 6 corresponds to scaling factors once the program requires SI units. After line 7, chord and incidence angles previously measured in different sections of the blade are inserted, so if we introduce the values of radial station and chord in meters and the incidence angle in degrees, scaling factors are 1.0; 1.0; 1.0. On the other hand, if it were required to introduce for example radial station and chord in millimeters and incidence angle in degrees the scaling factors would be 0.001; 0.001; 1.0. Line 7 corresponds to arbitrary constants that can be added to blade geometry, the first one referring to the radius station, second one to the chord, and third one to the incidence angle. In this project, the third constant is particularly important because it allows the user to study the propeller for variable pitch operational conditions by only modifying one value in the blade description, since a propeller will be studied for

different pitch operational conditions corresponding to a variation of incidence angle of -10°, -5°, 0°, 5° and 10°.

```
Camcarbon propeller

 2  0.1905        ! Nblades   line 1

 0.3415  6.5    ! CL0     CL_a   line 2
 -0.45  1.38    ! CLmin   CLmax   line 3

 0.01617  0.042  0.035  0.7594   !  CD0    CD2u  CD2l    CLCD0   line 4
 100000   -0.67        !  REref  REexp   line 5


 1.0  1.0   1.0  !  Rfac   Cfac   Bfac   line 6
 0.0     0.0      0.0  !  Radd   Cadd   Badd   line 7

#  r    chord    beta
 0.0405    0.02133    44.6101
 0.0505    0.02380    36.0936
 0.0605    0.02548    30.3462
 0.0705    0.02648    26.2016
 0.0805    0.02695    23.0688
 0.0905    0.02701    20.6161
 0.1005    0.02684    18.6428
 0.1105    0.02636    17.0201
 0.1205    0.02527    15.6618
 0.1305    0.02388    14.5079
 0.1405    0.02198    13.5151
 0.1505    0.02000    12.6519
 0.1605    0.01746    11.8942
 0.1705    0.01448    11.2237
 0.1805    0.01090    10.626
 0.1905    0.00087    10.09
```

Figure 3.6: QPROP Aeronaut Camcarbon 15x8 propeller input file

3.1.2.1 Camcarbon 15x8 airfoil characterization

Airfoil format data obtained from Web Plot Digitizer was imported to XFLR5 [25] and replicated with a smoother spline to be analyzed for a Reynolds number of 100000.

Most of the values required in the QPROP propeller input file to characterize the airfoil can be directly obtained from the XFLR5 C_l vs C_d and C_l vs α graphs (see Figure3.7 and Figure 3.8).

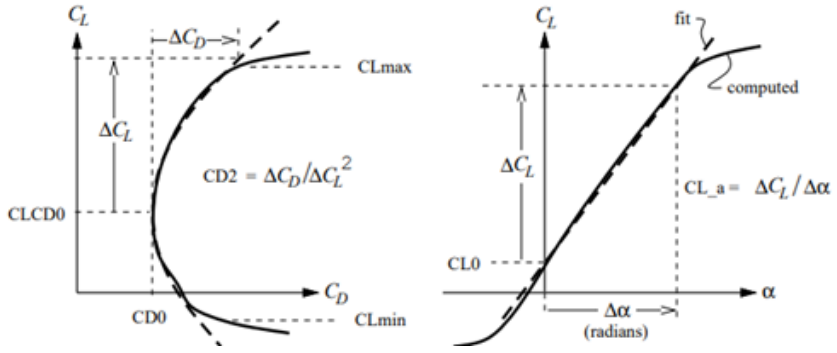

Figure 3.7: C_l vs C_d and C_l vs α graphs from [23] indicating corresponding value from propeller input file

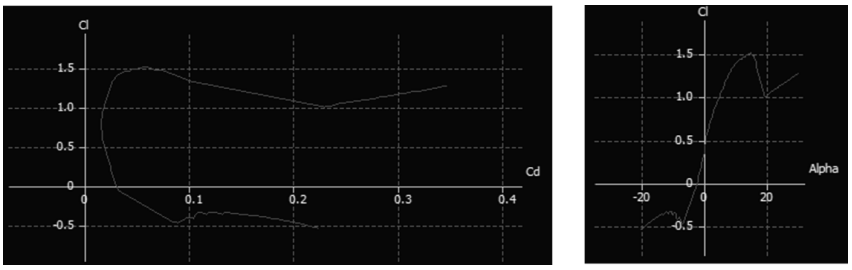

Figure 3.8: CL vs CD and CL vs α graphs of Aeronaut Camcarbon 15x8 airfoil at 0.75 blade radius.

Some values related to the airfoil performance present in propeller input file (Figure 3.6) are not implicit (such as C_{d2u} and C_{d2l} (line 4)), so XFOIL C_l vs C_d polar was compared with equations that QPROP [15] considers to obtain the parabola models. The process was made in an Excel file, where both XFOIL C_l vs C_d polar and a parabola related to the values inserted in propeller input file were overlapped in the same graph in such a way that by changing C_{d2u} and C_{d2l} it was possible to fit the parabola to the XFOIL polar (see Figure 3.9).

Furthermore, a XFOIL C_l vs C_d polar for the same airfoil but Reynolds number of 60000 was inserted in the same graph to evaluate the value of REexp (Figure 3.6 (line 5)) that would better adjust the parabola to other Reynolds numbers.

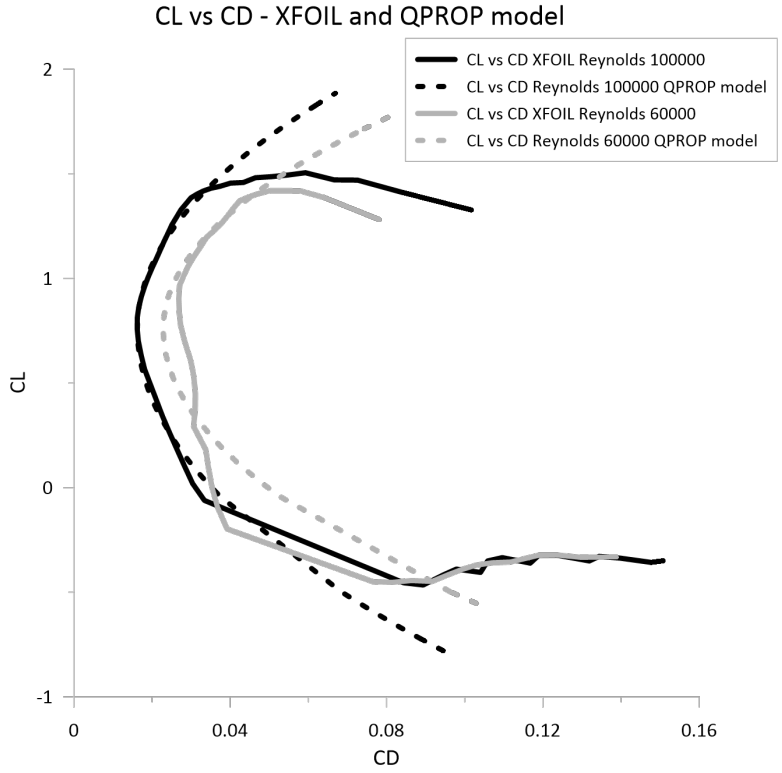

Figure 3.9: C_l vs C_d QPROP parabola model fitted with C_l vs C_d XFOIL polar for Reynolds number 100000 and 60000

3.2 Design concept

Using QMIL [16] different blade geometries were developed. The program generates the values of chord and incidence angle in different sections of a blade for Minimum Induced Loss conditions. A set of data related with airfoil to be used in the blade is defined in the propeller QMIL design input file. This includes C_l distribution along the blade and it is also possible to define power or thrust required for a certain value of relative wind speed and rotational speed. Different strategies were applied to generate a blade geometry that presents a suitable performance in variable pitch operational conditions.

3.2.1 Design Considerations

Using Aeronaut Camcarbon 15x8 as a term of comparison, the process to obtain a new propeller geometry followed different phases. The propeller radius value was settled the same (190.5mm) and beyond the airfoil measured in Aeronaut Camcarbon 15x8, s9000 airfoil was also considered in the development of a new propeller. Globally presenting better performance results in different stages of a variable pitch operational condition, s9000 airfoil was the one considered in the propeller design to apply additional modifications.

3.2.2 C_l distribution

Different distributions were tested to find a match between C_l distribution along the blade and the performance in a variable pitch operational condition. Thus, propellers with a C_l distribution along the blade equal to the maximum value of C_l/C_d of the airfoil [26] and using the maximum value of C_l for the respective airfoil until 80% of blade radius and lowest value in its tip [27] and [28] were considered design C_L distributions.

In the next chapter the numerical results seem to present satisfactory values when the distribution concerning the implementation of maximum C_l until 80% of blade radius and drastically decrease C_l in the tip is used with s9000 airfoil. To understand if this type of C_l distribution could still be improved, a sequence of minor changes in the C_l values were made until a distribution which presents better results was found. A series of propeller geometries were tested in QPROP and in those propellers the only change occurs in the distribution of C_l along the blade. Four values of C_lmax besides the value initially used were tested, until

100%, 90%, 80% and 70% of the radius position and C_l at the tip corresponding to 0, 0.2, 0.4, 0.5, 0.6, 0.8 1.0 or 1.2.

The power specified in all the designed propellers that is imposed in the execution of QMIL program was 90W for an airspeed of 3 m/s at 4000 rpm. This value was not used to improve propeller performance but as a neutral parameter so the propeller could use similar a amount of energy compared with Aeronaut Camcarbon 15x8 in different airspeeds and rotational speeds. A total of 75 propellers submitted to these modifications were analyzed in QPROP.

After performing a numerical analysis in QPROP of the QMIL generated propellers, one of them ($s9000_{14}$ with a C_l distribution of 1.2 until 80% of blade radius and 1.0 at the tip) was chosen for presenting the best global performance in variable pitch operational conditions to be manufactured in a 3D fused deposition modelling printer. Despite 3D printed propellers not having the same mechanical properties than the conventionally manufacturing techniques as injection-molded propeller, the accessible 3D FDM printing technology, low production cost and mainly the feasibility in the performance results are good reasons to choose this way of manufacturing propeller prototypes for wind tunnel performance testing.

3.2.3 Propeller Design Point

From the wind tunnel results of $s9000_{14}$ propeller that will be presented in Chapter 4, experimental results do not match the numerical results for different incidence angles at which the propeller was tested. As it will be explained later,this can be related to the 3D printing manufacturing propeller process but also with the fact that the propeller was designed with a C_l distribution nearly C_l maximum of the airfoil for 80% of radius. Despite that the numerical results present satisfactory performance values, the actual propeller can be facing stalling conditions.

Another propeller was designed to be 3D printed but this time with a C_l distribution corresponding to the best C_l/C_d of the airfoil. Furthermore, another factor was considered in the designing process of this new propeller. The design point in QMIL input file was settled as 4000 rpm at 11.5 m/s airspeed (airspeed of Aeronaut Camcarbon 15x8 propeller with maximum efficiency for 4000 rpm) and 120 W of specified power for this point.

To choose the specified power, different propellers were designed for the same parameters where the only difference was the design power. The chosen propeller was the one that presented greater performance than Aeronaut Camcarbon 15x8 in the variable pitch operational conditions according to the numerical study and, at the same time, the graph corresponding to thrust vs airspeed of maximum efficiency points in the same variable pitch operational conditions was an offset with higher thrust values than the equivalent graph from Aeronaut Camcarbon 15x8. Different parameters introduced in QMIL to generate the propeller ($s9000_{85}$) are represented in Figure 3.10.

```
Qmil propeller

 2     ! Nblades

 0.142  6.8   ! CL0     CL_a
 -0.35  1.18   ! CLmin   CLmax

 0.01673  0.08  0.016  0.711   !  CD0    CD2u  CD2l    CLCD0
 80000   -0.6        !  REref  REexp


  0.4  0.5  1.0   ! XIdes   (r/R locations where design cl is specified)
 0.86  0.86  0.86   ! CLdes   (specified cl)

 0.0405    !  hub radius(m)
 0.1905    !  tip radius(m)
 11.5   !  speed(m/s)
 4000   !  rpm

 0.0      !  Thrust(N)   ( 0 if power  specified )
 120    !  Power(W)    ( 0 if thrust specified )

0   0.2   ! Ldes    KQdes

 30       ! Nout    number of output stations (optional)
```

Figure 3.10: QMIL input file description to generate $s9000_{85}$ propeller

3.3 CAD model design

CAD models necessary to 3D print the selected propellers were developed in CATIA V5 based in the propellers geometry generated by QMIL. The output QMIL file presents 30 sections of the blade, each one with the respective chord and incidence angle. Due to limitations imposed by printer technical characteristics (maximum thickness that can be printed is 0.4 mm) the airfoil used in each one of the 30 sections is not the same as the one used in numerical studies. New airfoils were obtained identical to s9000 airfoil but with the desirable thickness of 0.4 mm at trailing edge using XFLR5 and defining a gap in trailing edge as a percentage of the chord in each section.

3.3.1 Determination of trailing edge position in each section

Most of the numerical data necessary to create the CAD model was obtained from the QMIL generated propeller geometry file and from the airfoil files exported from XFLR5. However, trailing edge position of each blade section also needs to be specified. Those points were calculated following the concept in which the center of mass of each blade section crosses the propeller plane of rotation.

Each blade section airfoil can be divided in smaller elements (see Figure 3.11)

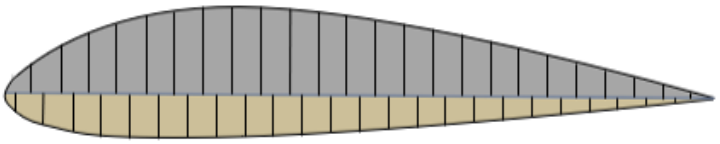

Figure 3.11: Representative picture of an airfoil divided in small elements.

Each element has an area that can be calculated by the absolute value of the difference between two consecutive abscissas with the absolute value of the corresponding ordinates average.

With the area of each element, the center of area can be calculated by:

$$x_{ca} = \Sigma \left(A_i \times x_i \right) / \Sigma A_i \quad (3.2)$$

$$y_{ca} = \Sigma \left(A_i \times y_i \right) / \Sigma A_i \quad (3.3)$$

The variables needed to calculate the trailing edge position are identified in the following Figure 3.12:

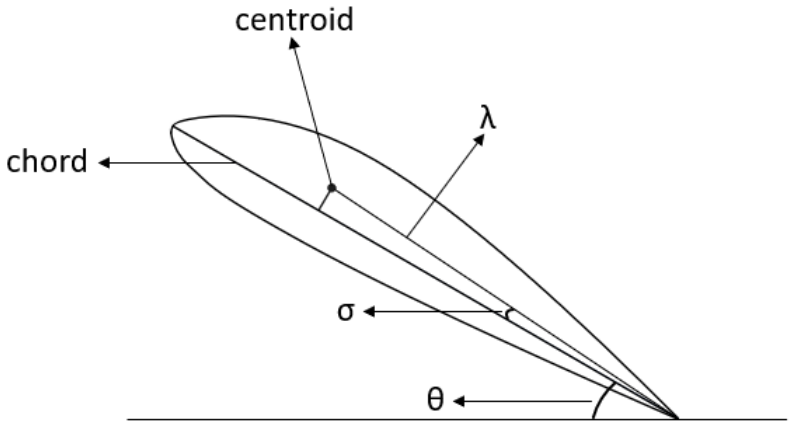

Figure 3.12: Representative picture of centroid, angles and distance of trailing edge

1. θ represents the angle of incidence of the section that is directly specified in QMIL output file;

2. λ is the hypotenuse length of the triangle formed by the centroid, chord and trailing edge point;

3. σ is the angle between chord and λ

$$x_{trailing\ edge} = \lambda \cos(\sigma+\theta) \quad (3.4)$$

$$y_{trailing\ edge} = -\lambda \sin(\sigma+\theta) \quad (3.5)$$

σ and λ can be calculated using the calculated position of center of mass:

$$\tan\sigma = \frac{y_{ca}}{1 - x_{ca}} \quad (3.6)$$

$$\lambda = c\sqrt{(y_{ca})^2 + (1 - x_{ca})^2} \quad (3.7)$$

For this specific case, as each section was drawn with an airfoil with 0.4 mm thickness in the trailing edge, another correction factor was considered to find the exact position of the two

points that compose the trailing edge.

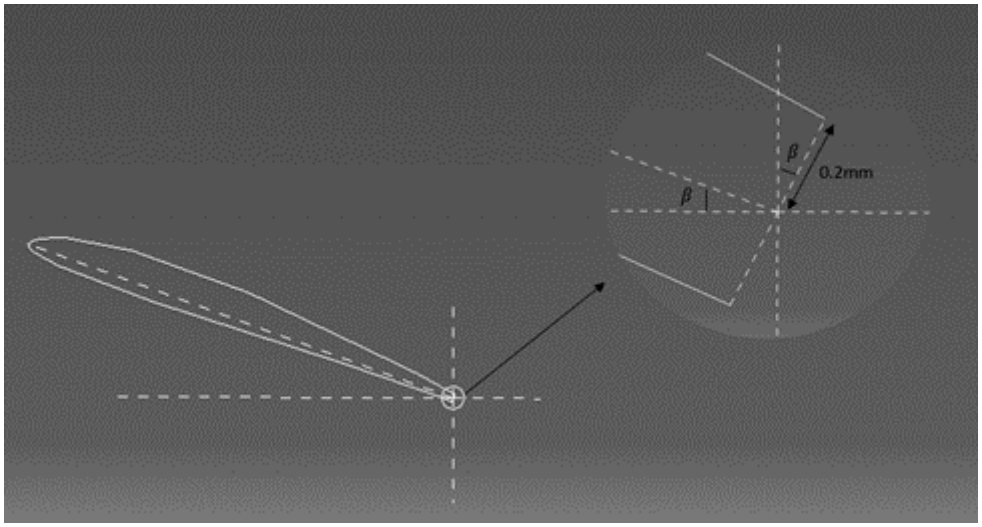

Figure 3.13: Trailing edge gap specifications

Considering 0.4 mm gap in trailing edge and noting that each airfoil section starts to be drawn in the upper point of trailing edge, the coordinates specified in trailing edge field are:

$$x_{trailing\ edge} = \lambda \cos(\sigma+\theta) + 0.2 \sin(\theta) \quad (3.8)$$

$$y_{trailing\ edge} = -\lambda \sin(\sigma+\theta) + 0.2 \cos(\theta) \quad (3.9)$$

3.3.2 Blade propeller 3D modelling

An Excel file in which the necessary input data are the radial position of each section, the respective general coordinates of the airfoil, chord value (c), incidence angle (θ) and the exact position of trailing edge was developed to generate each blade propeller section.

For each section the process is similar:

1. **Scale**

   Each coordinate of the airfoil was multiplied by the chord value to get a new airfoil with the section dimension. The abscissa and ordinate of the corresponding points will be represented by X and Y, respectively.

2. **Rotation**

A position vector was defined to determine the new points after the rotation corresponding to the incidence angle was applied:

L is the vector length corresponding to the distance of the airfoil point to the axes origin (0,0).

$$L = \sqrt{X^2 + Y^2} \quad (3.10)$$

γ is the angle between position vector and abscissa's axis.

$$\gamma = \tan^{-1}(Y/X) \quad (3.11)$$

Considering the rotation corresponding to the incidence angle, $X_{rotated}$ and $Y_{rotated}$ were calculated.

$$X_{rotated} = L\cos(\gamma - \theta) \quad (3.12)$$

$$Y_{rotated} = L\sin(\gamma - \theta) \quad (3.13)$$

3. **Translation**

A constant to get the airfoil in the desired position (in this case the goal was to have center of mass of each section crossing the propeller plane of rotation and aligned with the radial direction along the blade) was added to the rotated coordinates. Previously calculated values of the section trailing edge were used for this situation.

$$D_X = X_{trailing\ edge\ final} - X_{trailing\ edge\ rotated} \quad (3.14)$$

$$D_Y = Y_{trailing\ edge\ final} - Y_{trailing\ edge\ rotated} \quad (3.15)$$

Final values of section points were then calculated:

$$X_{final} = X_{rotated} + D_X \quad (3.16)$$

$$Y_{final} = Y_{rotated} + D_Y \quad (3.17)$$

Considering the three dimensional case, the value of the third coordinate of each point coincides with the radius position of the section where that point is inserted. Using a macro tool, the defined points were used to directly create splines in CATIA V5 corresponding to the airfoil in each section. (Figure 3.14)

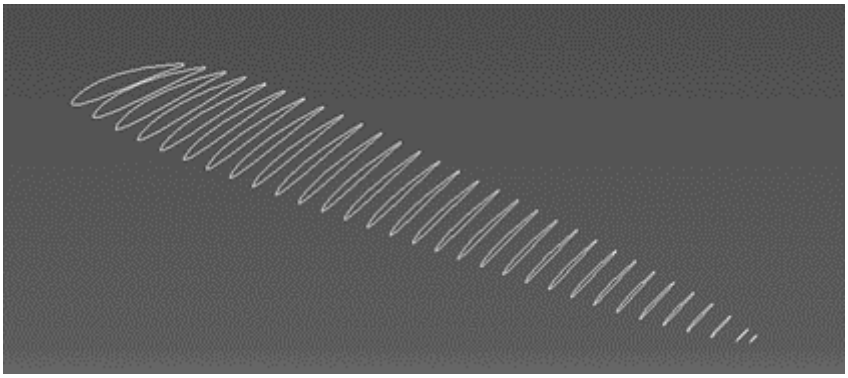

Figure 3.14: Splines created using Excel macro tool corresponding to $s9000_{85}$ blade airfoil in each section

Finally, to create the blade structure the "multi-sections solid" tool was used with all the sections splines (Figure 3.15).

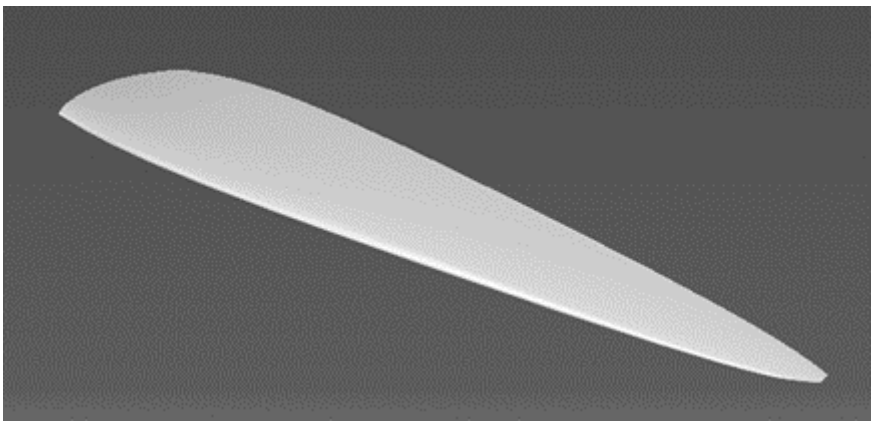

Figure 3.15: $s9000_{85}$ blade structure

3.3.3 Propeller Supporting Structure

Due to the accuracy imposed in the printing process of a propeller, a structure with supporting purposes was also included in the CAD model. This structure is a solid object with a tangent interface connection with the blade leading edge along its span. A border surface that could easily be removed from the supporting object was required and since the trailing edge is featured by its thin thickness, the leading edge was chosen as the surface to be sustained by the support structure.

3.4 3D Propeller Printing and Finishing Procedure

Both $s9000_{14}$ and $s9000_{85}$ propellers were printed and tested in the wind tunnel with the blades in three different pitch setting incidence positions ($\Delta\beta = -10$, $\Delta\beta = 0$, $\Delta\beta = +10$ degrees) as propeller blade incidence angle to study the performance in variable pitch operational conditions.

Six blades were printed to study the $s9000_{14}$ propeller. For each incidence angle studied, two similar blades with the respective incidence angle were printed and fixed to a hub. In $s9000_{85}$ propeller study only two blades were printed but in this case three different hubs were designed to analyze the propeller in the three different pitch setting angular positions (Figure 3.16).

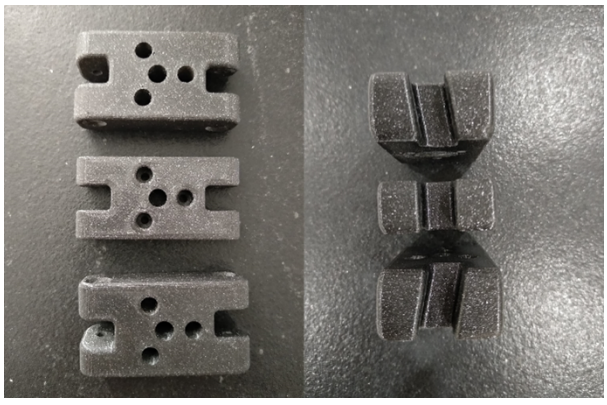

Figure 3.16: Hubs front view (left) and side view (right) used to change the incidence angle of $s9000_{85}$ propeller for a variation of -10, 0 and +10 degrees respectively

All the propeller blades were printed on a Prusa MK3S FDM 3D printer and the material used was the Polylactic acid (PLA), one of the most common and cheapest materials. An infill of

100% was used to get the stiffest propeller blades possible with the printed material.

3.4.1 3D Propeller Finishing

The different blades of $s9000_{14}$ were printed and separated from their respective supporting structures using an utility knife and then with the same tool the surface was scraped to remove the visible roughness. Next, the blades were sanded with a fine sandpaper, painted with a clear coating and sanded again to achieve a smother surface. For each of the three printed propellers, both blades were weighted in a precision balance evaluating the similarity between them. The results were not the same. The blades' weights presented small variations. Looking for more accurate results and to prevent vibrations in the wind tunnel test the heavier blade was scraped near the root until it got the same weight as the other blade. Using a similar procedure, the blades were scraped to obtain the same center of mass position along the blades radius. The only difference in the finishing process of $s9000_{85}$ is that unlike $s9000_{14}$, this one was not painted.

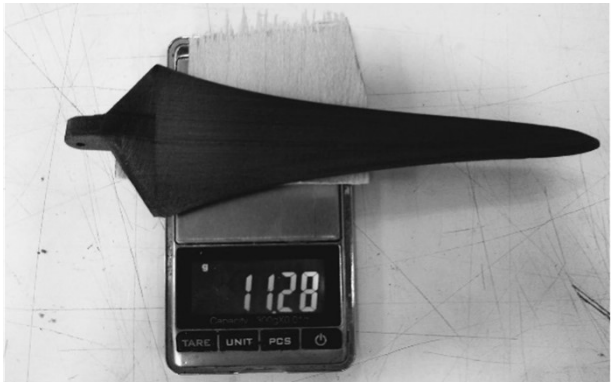

Figure 3.17: $S9000_{14}$ propeller $\Delta\beta$= -10º adjustment being weighted in a precision balance

3.5 3D Printed Propellers Prototypes

In addition to the propellers $s9000_{14}$ and $s9000_{85}$ designed to be used in a variable pitch mechanism, other types of propellers were also 3D printed to be tested in the wind tunnel.

In [29] the use of accessible 3D FDM printing technology as a way of rapid prototyping low Reynolds number UAV propeller geometries was studied. QPROP was used to predict propeller performance of an established propeller design. Propeller geometry was replicated in a CAD model design and different strategies considering the blade printing orientation were

tested to achieve the most accurate print. On the first attempts, the blade trailing edge was facing the printing bed to avoid the removal of leading edge from the supporter structures. Due to its tiny thickness, the contact area was not enough to support the blade structure leading to printing failures. This way, a supporting structure to support the leading edge over a tangent interface along the blade span was modeled. The blades were printed using PLA filament, 100% infill and an extrusion width as small as possible to achieve the most possible precision (0.4 mm).

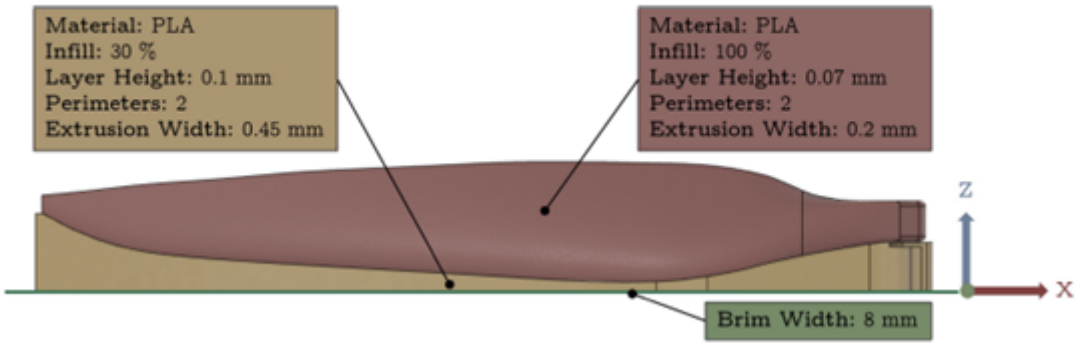

Figure 3.18: Model orientation of blade and support structure; Printing settings applied to the different components [29]

Four identical blades were printed to create two identical propellers. The blades of one of the propellers were submitted to a light scraping with an utility knife. The blades of the other propeller were submitted to a major finishing to obtain a smooth surface. In this case the blades were extensively scraped, sanded and painted with two layers of clear coating. Both propellers were tested in the wind tunnel and the difference between numerical and experimental results will be compared in Chapter 4 with the same difference in the propellers developed for a variable pitch mechanism once the same numerical program (QPROP) and similar printing techniques in the propeller prototypes tested in the wind tunnel were used.

3.6 Wind tunnel testing

With all the blades printed and finished, all the propellers were tested in the University of Beira Interior (UBI) subsonic wind tunnel (see Figure 3.19) where a low Reynolds number propeller performance test rig is installed (see Section 3.6.1) .

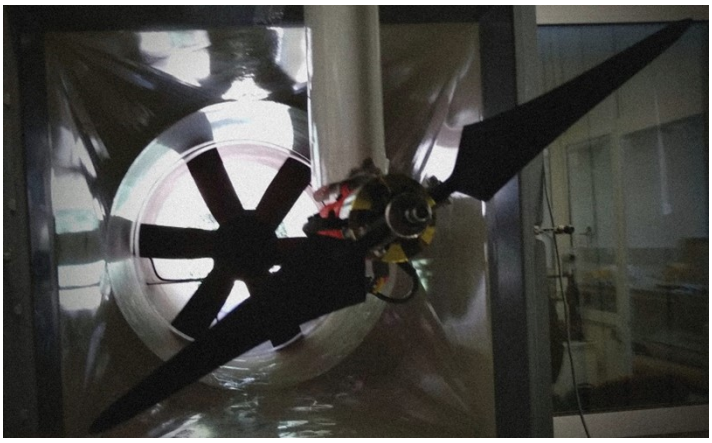

Figure 3.19: Propeller $s9000_{14}$ positioned to be tested in UBI subsonic wind tunnel

3.6.1 Low Reynolds Number Propeller Performance Test Rig

The low Reynolds number propeller performance test rig developed by Pedro Alves [30] was used to measure the performance of the printed propellers in the wind tunnel.

The test rig mechanism to measure the thrust force was designed as a T-shaped pendulum positioned to have the thrust vector at the center of the wind tunnel test section and making use of the free space in the wind tunnel upper wall to place the thrust load cell, reducing measuring disturbances associated to a complex setting arrangement inside the test section.

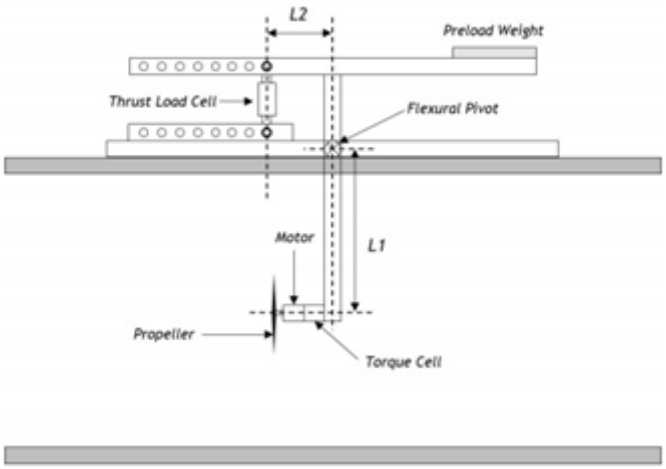

Figure 3.20: Low Reynolds Number Propeller Performance Test Rig [11]

A thrust load cell FN3148 manufactured by FGP Sensors & Instrumentation and torque transducers RTS-100 or RTS-200 manufactured by Transducer Techniques are connected to SCB-

68 strain gauge manufactured by Mantracourt responsible to create a high precision electrical signal proportional to the measured force.

3.6.2 Propeller and Freestream Speed Measurement

A Fairchild Semiconductor QRD1114 photo-reflector that counts the number of revolutions that the output shaft does in a fixed period was used to measure the propeller rotational speed.

The freestream wind tunnel airspeed was measured using the values of a combination of sensors in different locations along the wind tunnel. MKS Instruments 226A Baratron differential pressure transducer, a National Instruments LM335 thermocouple used in two static pressure ports (one at the settling chamber and another in the entrance of the test section as shown in Figure 3.20) as well as an absolute pressure transducer MPXA4115A manufactured by Freescale Semiconductor (used to measure the atmospheric pressure outside the tunnel) provide the values to calculate the velocity in the test section using Bernoulli's equation.

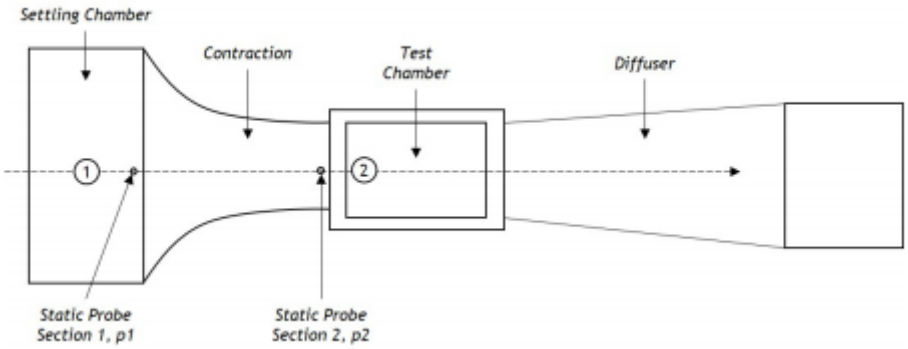

Figure 3.21: Wind tunnel configuration and static probe location [30]

$$\frac{p_1}{\rho_2} + \frac{1}{2}{V_1}^2 + gz_1 = \frac{p_2}{\rho} + \frac{1}{2}{V_2}^2 + gz_2 \quad (3.18)$$

Considering the horizontal tunnel $z_1 = z_2$

$${V_2}^2 - {V_1}^2 = \frac{2(p_1 - p_2)}{\rho} \quad (3.19)$$

The incompressible continuity relationship:

$$A_1 V_1 = A_2 V_2 \quad (3.20)$$

$$V_1 = \frac{A_2}{A_1} V_2 \quad (3.21)$$

Combining Equations 3.19 and 3.21 the velocity in the test section is given by:

$$V_2 = \sqrt{\frac{2(p_1 - p_2)}{\rho \left[1 - \left(\frac{A_2}{A_1}\right)^2\right]}} \quad (3.22)$$

Chapter 4

Results and discussion

4.1 Aeronaut Camcarbon 15x8 Numerical Study

Based on the propeller measurement explained in Section 3.1, the existing Aeronaut Camcarbon 15x8 propeller was analyzed in QPROP for variable pitch operational conditions. The maximum efficiency of the propeller applying variations in its pitch angle is represented in the graph of Figure 4.1. It is evident from this data that the maximum efficiency of Aeronaut Camcarbon 15x8 increases when the blade incidence angle increases. The maximum propulsive efficiency increases faster at lower incidence angles. This means the curve gradient is larger at low incidences and decreases as incidence increases. E. g., from $\Delta\beta = -10^{o}$ to $\Delta\beta = -5^{o}$ the maximum efficiency increases 27%, while from $\Delta\beta = +5^{o}$ to $\Delta\beta = +10^{o}$ the maximum efficiency only improves 3%.

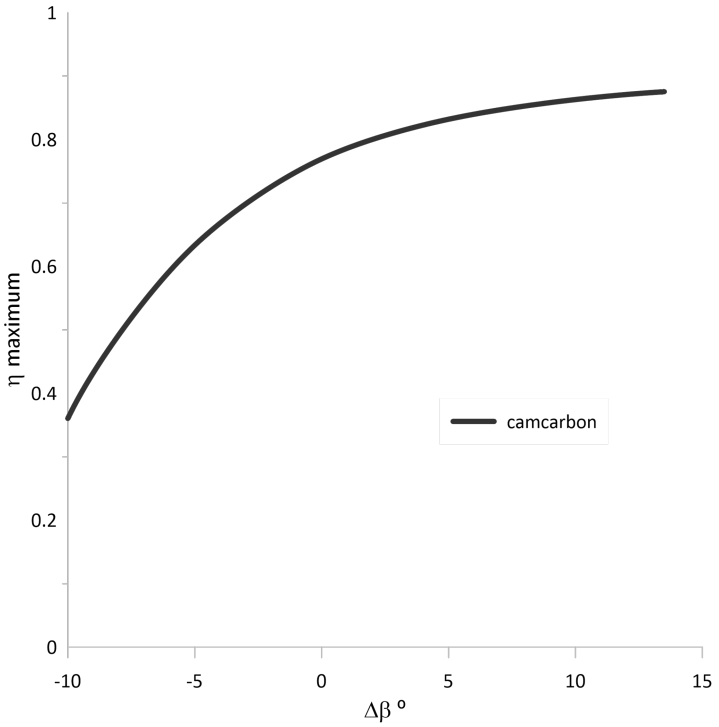

Figure 4.1: Maximum efficiency vs pitch incidence angle variation of Aeronaut Camcarbon 15x8 propeller at 8000rpm

4.2 Airfoil Selection

A comparison between the Aeronaut Camcarbon 15x8, a propeller with s9000 airfoil and another propeller with the Aeronaut Camcarbon 15x8 airfoil but designed with the same concept of setting the lift coefficient for the airfoil maximum lift to drag ratio in the design pitch incidence angle as the s9000 airfoil propeller is presented in Figures 4.2, 4.3 to investigate if using the s9000 airfoil could bring performance benefits in the variable pitch operational conditions in study.

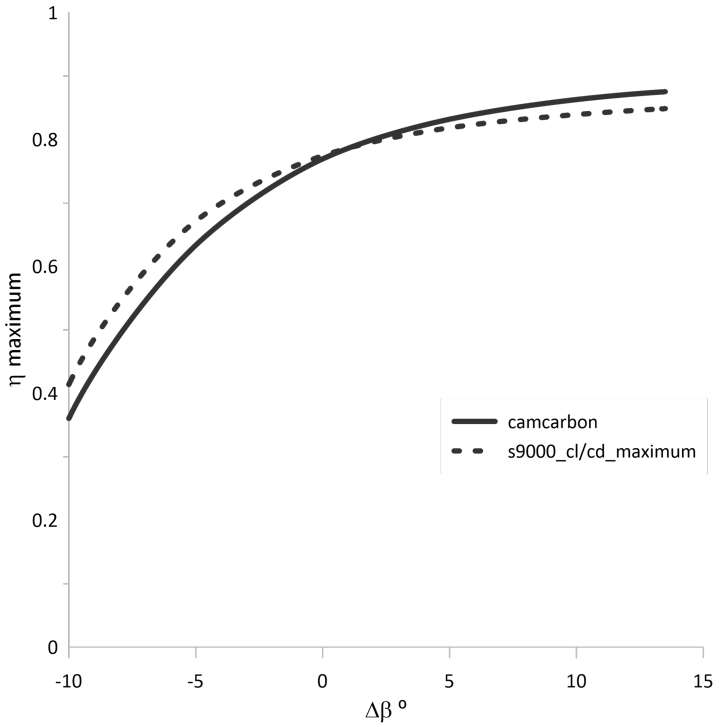

Figure 4.2: Maximum efficiency of Aeronaut Camcarbon 15x8 and s9000_cl/cd_maximum for each variation of pitch incidence angle values (8000 rpm)

It can be realized, through figure 4.2, that a slight improvement of the propeller maximum efficiency exists with the airfoil s9000 when the propeller is used in a low pitch blade incidence angle position. However, the maximum efficiency for a coarse pitch condition decreases when compared with the Aeronaut Camcarbon 15x8.

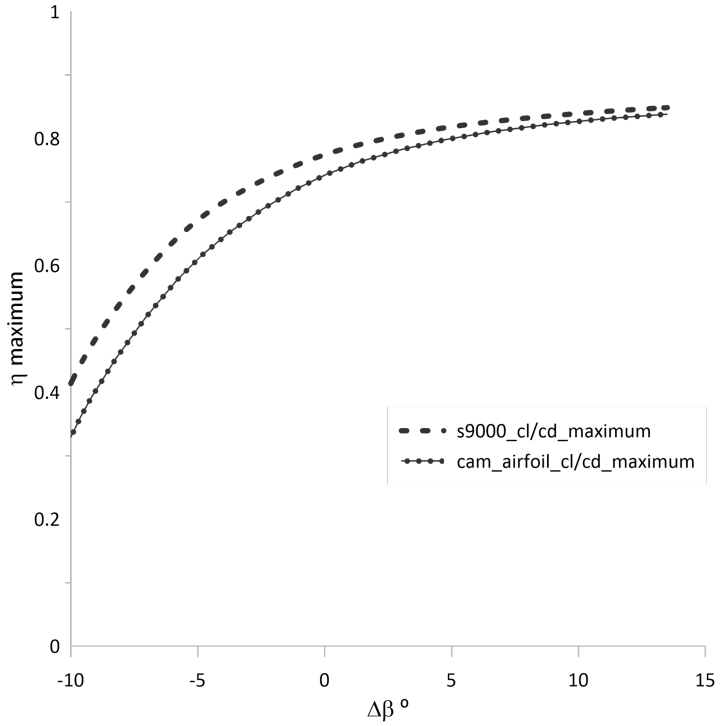

Figure 4.3: Maximum efficiency of s9000_cl/cd_maximum and cam_airfoil_cl/cd_maximum for each variation of pitch incidence angle values (8000 rpm)

In Figure 4.3 the previous propeller with s9000 airfoil is compared with another propeller using the Aeronaut Camcarbon 15x8 airfoil at 0.75 radius, both following the same concept of C_l distribution along the blade. Between both propellers designed over the same concept, it seems that the one with s9000 airfoil presents better performance overall.

4.3 Numerical Study of Propellers Designed with Different Lift Coefficient Distributions

Using s9000 airfoil, different C_l distributions are used to design propellers and consequently identify which one presents better results in variable pitch operational conditions. Another design alternative is a propeller blade designed to hold maximum C_l (1.2 for the s9000 airfoil) until 80% of radius and then linearly dropping to a very low value at the tip (0.4). This propeller is designated by $s9000_3$.

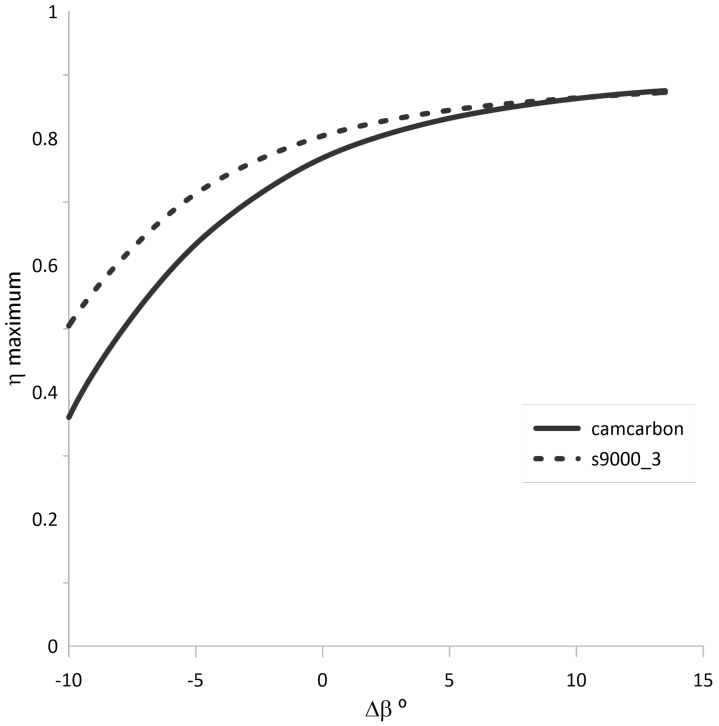

Figure 4.4: Maximum efficiency of Aeronaut Camcarbon 15x8 and $s9000_3$ for each variation of pitch incidence angle values (8000 rpm)

The results of $s9000_3$ analysis compared with the benchmarking Aeronaut 15x8 propeller blade are seen in Figure 4.4 to show encouraging results for all $\Delta\beta$ interval. Considering coarse pitch condition (especially for $\Delta\beta = +10^{o}$ and $\Delta\beta = +13.5^{o}$) $s9000_3$ propeller presents very similar maximum efficiencies compared with Aeronaut Camcarbon 15x8. For all the other $\Delta\beta$ lower values, $s9000_3$ presents better performance than Aeronaut Camcarbon 15x8, being this difference more emphasized the lower the value of $\Delta\beta$.

Despite this propeller presenting encouraging results to be used in a variable pitch mechanism, other propellers were designed following a similar concept of C_l distribution along the blade but with small changes. From the 75 different propeller blades that were designed, the highest values of the maximum efficiency in each $\Delta\beta$ position are presented in the Table 4.1.

$\Delta\beta$ º	Propeller	C_l distribution along the blade [$\mathbf{C_l(r/R)}$]	Maximum efficiency
-10	S9000_10	1.2(0.3), 1.2(0.8), 1.2(1)	0.5960
-5	S9000_10	1.2(0.3), 1.2(0.8), 1.2(1)	0.7483
0	S9000_26	1.27(0.3), 1.27(0.8), 1.0(1)	0.8133
+5	S9000_29	1.2(0.3), 1.2(0.7), 0.8(1)	0.8465
+10	S9000_27	1.2(0.3), 1.2(0.7), 0.4(1)	0.8657
+13.5	S9000_27	1.2(0.3), 1.2(0.7), 0.4(1)	0.8747

Table 4.1: Maximum efficiency and C_l distribution along the blade of propellers with higher efficiency between all the propellers with s9000 airfoil for a certain value of $\Delta\beta$

The propeller blade that was chosen to be 3D printed to continue with the experimental study is the one design which presents the most consistent values of maximum efficiency and closer to the highest overall in $\Delta\beta = \{-10, -5, 0, +5, +10, +13.5\}$ interval. Using that concept, propeller chosen is $s9000_{14}$. The results for the maximum efficiency of $s9000_{14}$ propeller for this $\Delta\beta$ interval are presented in Table 4.2 and Figure 4.5.

$\Delta\beta$ º	Propeller	C_l distribution along the blade [$\mathbf{C_l(r/R)}$]	Maximum efficiency
-10	S9000_14	1.2(0.3),1.2(0.8),1.0(1)	0.5821
-5			0.7441
0			0.8131
+5			0.8447
+10			0.8602
+13.5			0.8671

Table 4.2: Maximum efficiency and cl distribution along the blade of propellers with higher efficiency between all the propellers with s9000 airfoil for a certain value of $\Delta\beta$

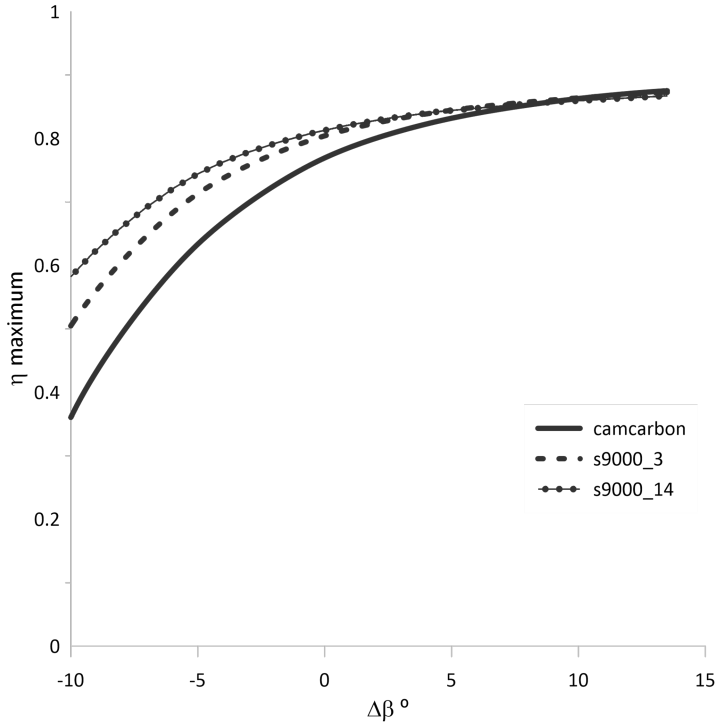

Figure 4.5: Maximum efficiency of Aeronaut Camcarbon 15x8, $s9000_3$ and $s9000_{14}$ for each variation of pitch incidence angle values (8000 rpm)

In Figure 4.5, plotted against the results for Aeronaut Camcarbon 15x8, $s9000_3$ propeller blade designs for a comparison with the chosen $s9000_{14}$. From this data, it is apparent that $s9000_{14}$ is the most efficient of the three propellers blades designs when it is used in a low pitch condition. Still considering the low pitch condition, the difference of maximum efficiency between $s9000_{14}$ and $s9000_3$ is lower than the difference between Aeronaut Camcar-

bon 15x8 and $s9000_{14}$ or $s9000_3$. When it starts to be used in a coarser pitch condition, the increasing ratio of maximum efficiency from $s9000_{14}$ is lower comparing with $s9000_3$ which in turn is lower than Aeronaut Camcarbon 15x8. This way, for a pitch corresponding to $\Delta\beta$ = $+13.5^{o}$, the maximum efficiency of Aeronaut Camcarbon 15x8 is slightly superior to $s9000_3$ and $s9000_{14}$.

Due to restrictions imposed by the 3D FDM printer, the numerical designed tested propellers cannot be exactly replicated to be built by the 3D printer for testing in the wind tunnel. The most significant adjustment required to be done in the propeller design is to increase the trailing edge thickness, which needs to have a minimum value of 0.4 mm (the diameter of the fused filament extrusion nozzle of the 3D printer in use throughout the work). Applying that adjustment, the maximum theoretical efficiency of numerically simulated $s9000_{14}$ for the $\Delta\beta$ interval values is presented in Figure 4.6

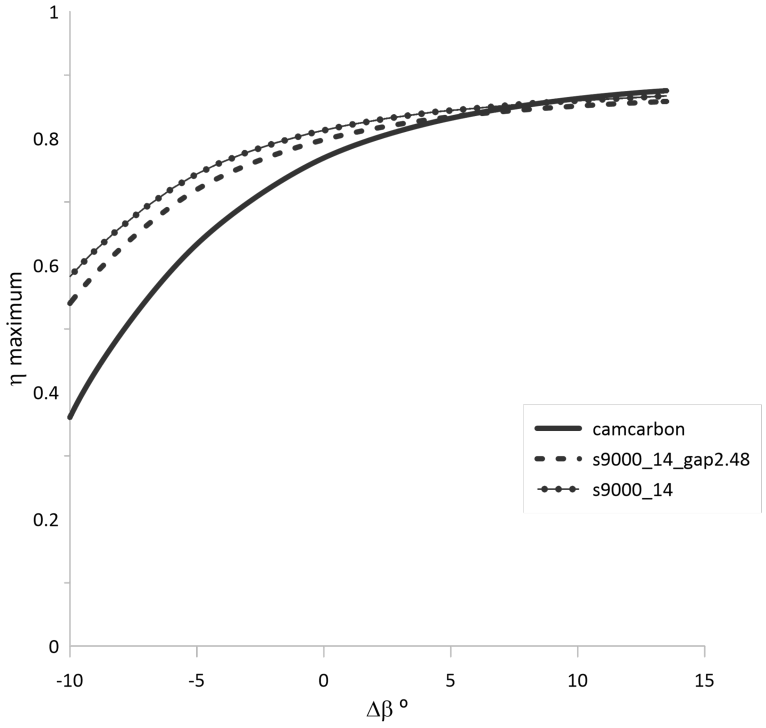

Figure 4.6: Maximum efficiency of Aeronaut Camcarbon 15x8, $s9000_{14}$ and $s9000_{14}$ suitable for printing ($s9000_{14}$_gap2.48) for each variation of pitch incidence angle values (8000 rpm)

As seen, the maximum efficiency obtained in QPROP of $s9000_{14}$ applying the required modifications to be 3D printed presents lower values compared with the original propeller. The difference is bigger for low pitch conditions.

4.4 Numerical Study of the $S9000_{14}$ Propeller Blade Design

From here on, the $s9000_{14}$ is considered the final propeller designed with the geometrical adjustments required to be 3D printed. Three propellers were printed varying only the incidence angle set at the root of the blade, so that $s9000_{14}$ could be tested in the wind tunnel for variable pitch conditions with a single folding blades propeller holding hub corresponding to low, design and high pitch incidence angle, $\Delta\beta = -10^{o}$, $\Delta\beta = 0^{o}$ and $\Delta\beta = +10^{o}$ respectively.

4.4.1 Low Pitch Setting: $\Delta\beta = -10^{o}$

In Figures 4.7, 4.8 and 4.9 the performance results of $s9000_{14}$, used with a pitch incidence angle variation of -10 degrees considering its original design pitch, obtained from QPROP and wind tunnel when it was tested at three different rotational speeds are compared. In each figure the thrust coefficient (a), power coefficient (b) and propulsive efficiency (c) of the propeller as functions of advance ratio is represented.

As seen in Figure 4.7 (a), maximum efficiency obtained in wind tunnel of s9000_14 propeller tested for a low pitch condition ($\Delta\beta = -10$ is higher than the prediction obtained in QPROP at 3000rpm. At 4000rpm the propeller presented some vibration during the wind tunnel test and it was not possible to continue the test for higher advance ratio values. Nevertheless, propeller maximum efficiency, obtained from wind tunnel data at 4000 rpm are at least as high as the numerical predicted (see Figure 4.7 (b)). At 5000 rpm, the maximum measured efficiency is slightly lower than the QPROP prediction as it is verified in the results presented of the test at 5000rpm (see Figure 4.7 (c)). It is also important to note that for all the three rotational speeds tested, the values of the maximum efficiency values obtained by wind tunnel data takes place for an advance ratio slightly higher than the predicted by QPROP. Thrust and power coefficient are directly related to the propeller efficiency. The higher the value of rotational speed, the higher the gap of thrust coefficient and power coefficient values between QPROP and wind tunnel data, where the values obtained from wind tunnel data are larger than QPROP prediction except for 3000 rpm. As the difference of power coefficient obtained from wind tunnel and QPROP data is larger at higher revolutions compared with the difference of thrust coefficient, propeller efficiency calculated from wind tunnel data starts to decrease compared with that obtained with QPROP as the rotational speed is increased during the wind tunnel tests.

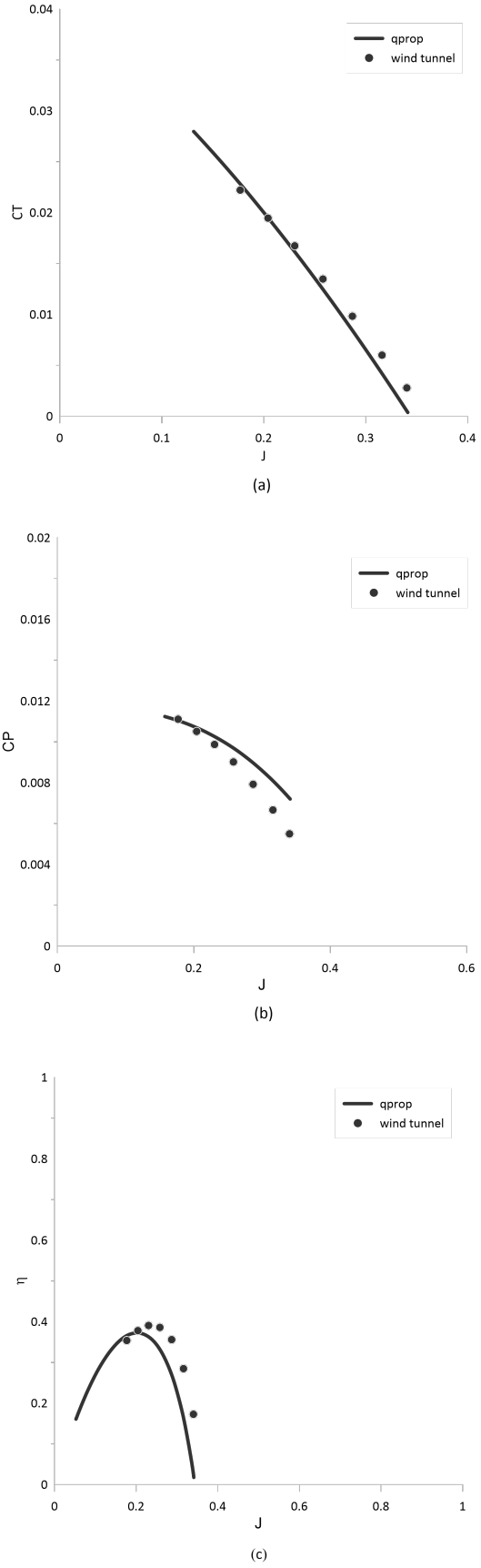

Figure 4.7: Thrust coefficient (a), power coefficient (b) and efficiency (c) vs advance ratio of $s9000_{14}$ propeller for $\Delta\beta$ variation of -10° at 3000 rpm

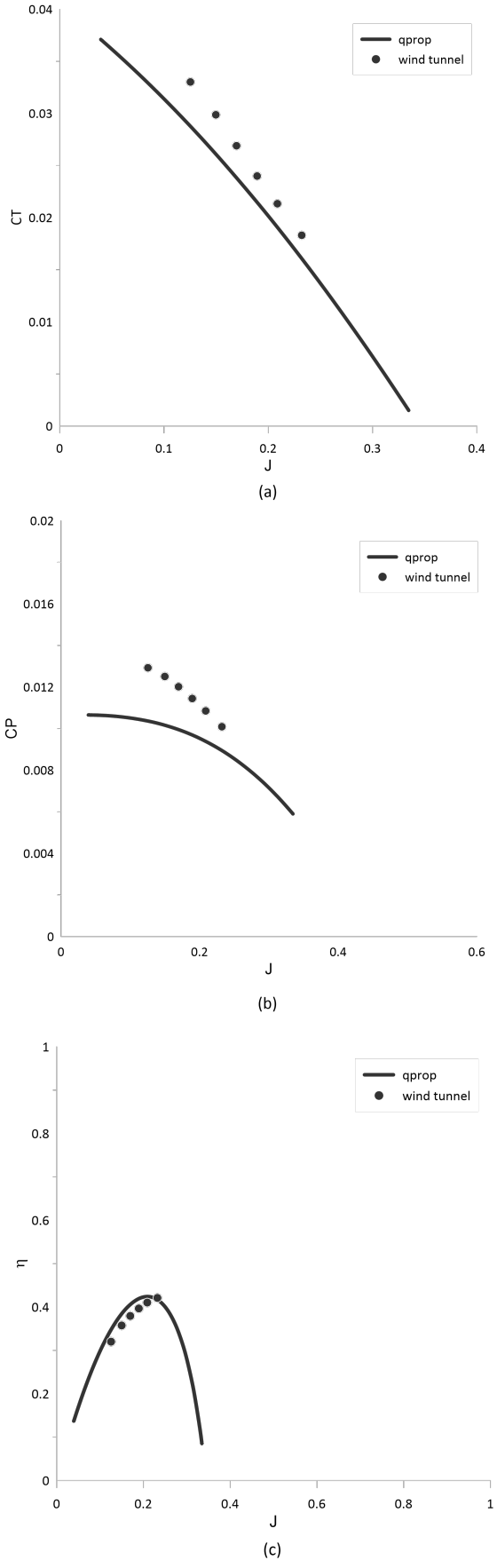

Figure 4.8: Thrust coefficient (a), power coefficient (b) and efficiency (c) vs advance ratio of $s9000_{14}$ propeller for $\Delta\beta$ variation of -10º at 4000 rpm

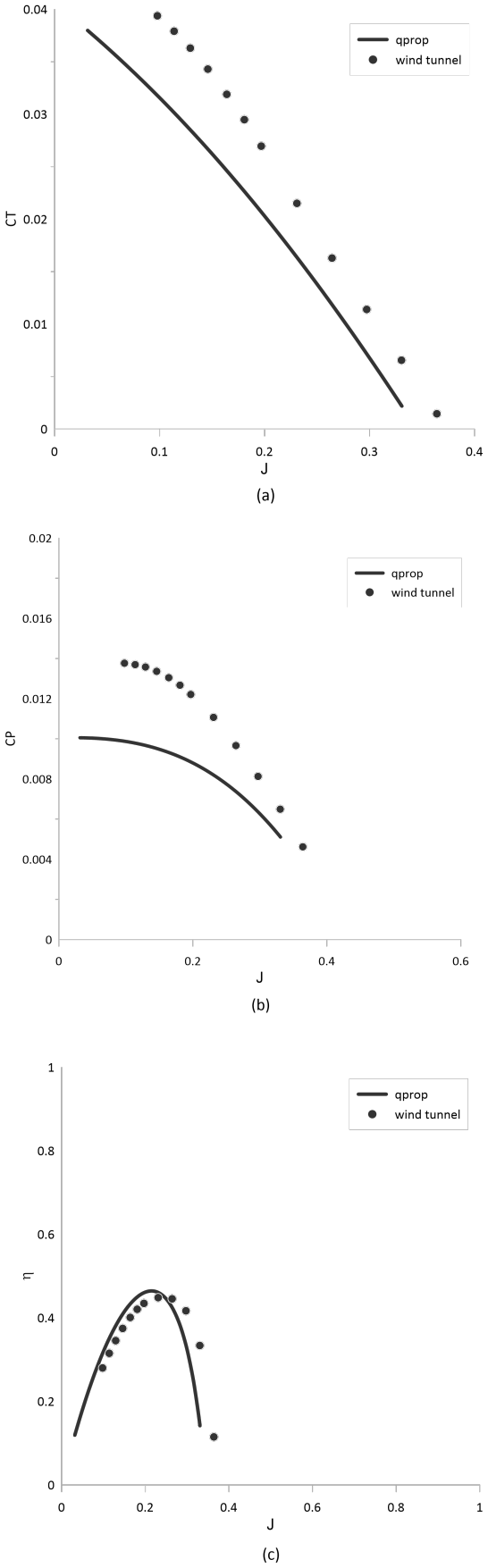

Figure 4.9: Thrust coefficient (a), power coefficient (b) and efficiency (c) vs advance ratio of $s9000_{14}$ propeller for $\Delta\beta$ variation of -10° at 5000 rpm

4.4.2 Design Pitch Setting: $\Delta\beta = 0^{o}$

In Figures 4.10, 4.11 and 4.12 the performance results of $s9000_{14}$, used with its designed pitch, obtained from QPROP and wind tunnel when it was tested at three different rotational speeds are compared. In each figure the thrust coefficient (a), power coefficient (b) and propulsive efficiency (c) of the propeller as functions of advance ratio is represented.

As seen in Figures 4.10 (c), 4.11 (c) and 4.12 (c), considering the propeller used with no variation of its original design pitch, the maximum efficiency obtained from wind tunnel tests data is lower than that predicted by QPROP for the three values of tested rotational speed. Analyzing the main variables that define the propeller efficiency (thrust coefficient, power coefficient and advance ratio), the thrust coefficient presents a relatively similar curve to the one predicted by QPROP, however the same thing does not happen for the power coefficient. At 3000 rpm, the graph of thrust coefficient obtained from the wind tunnel data is similar with the one obtained with QPROP, however the required power for the propeller to produce that thrust is higher than the predicted as it can be seen in Figure 4.10 (b). At 4000 rpm, thrust coefficient calculated from the wind tunnel results is slightly higher than predicted by QPROP simulations except for advance ratio values lower than 0.3. That evidence is not an issue since the propeller with this pitch is not expected to be used for the low airspeed velocities at 4000 rpm corresponding to advance ratio values lower than 0.3. However the high values of power required to achieve that amount of thrust is negatively affecting the efficiency of the propeller compared with QPROP results. At 5000 rpm the relation between thrust and power coefficient is similar with the test at 4000 rpm but the gap between QPROP predictions and wind tunnel data is even higher.

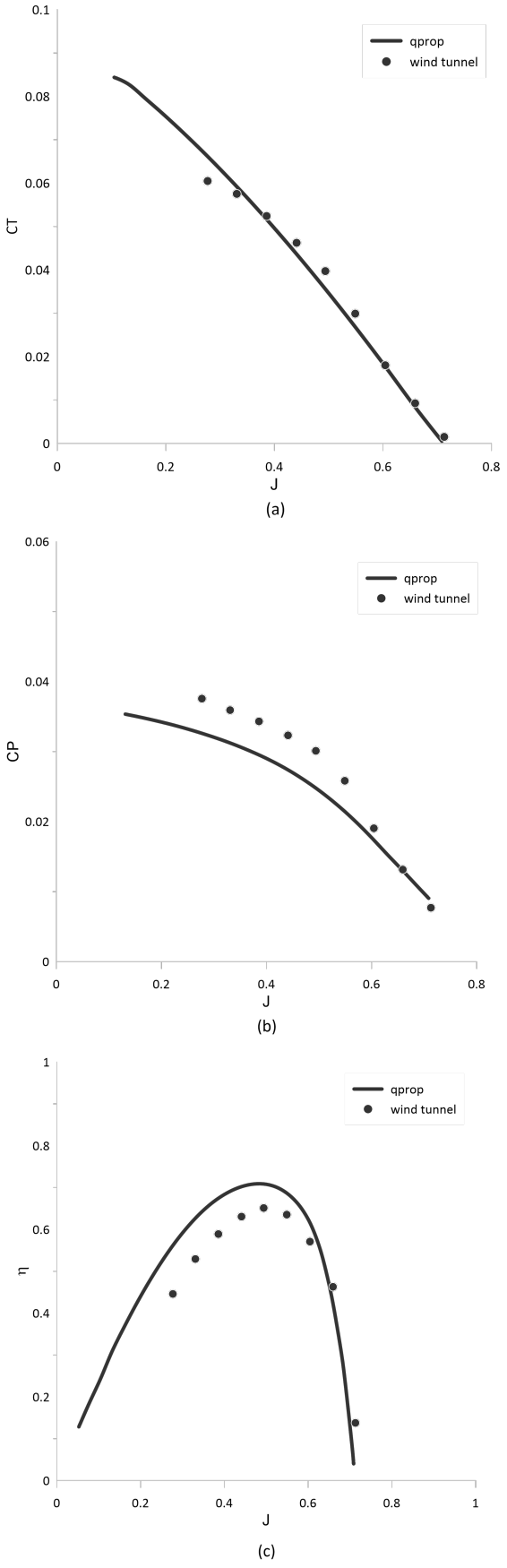

Figure 4.10: Thrust coefficient (a), power coefficient (b) and efficiency (c) vs advance ratio of $s9000_{14}$ propeller with no variation of its original pitch at 3000 rpm

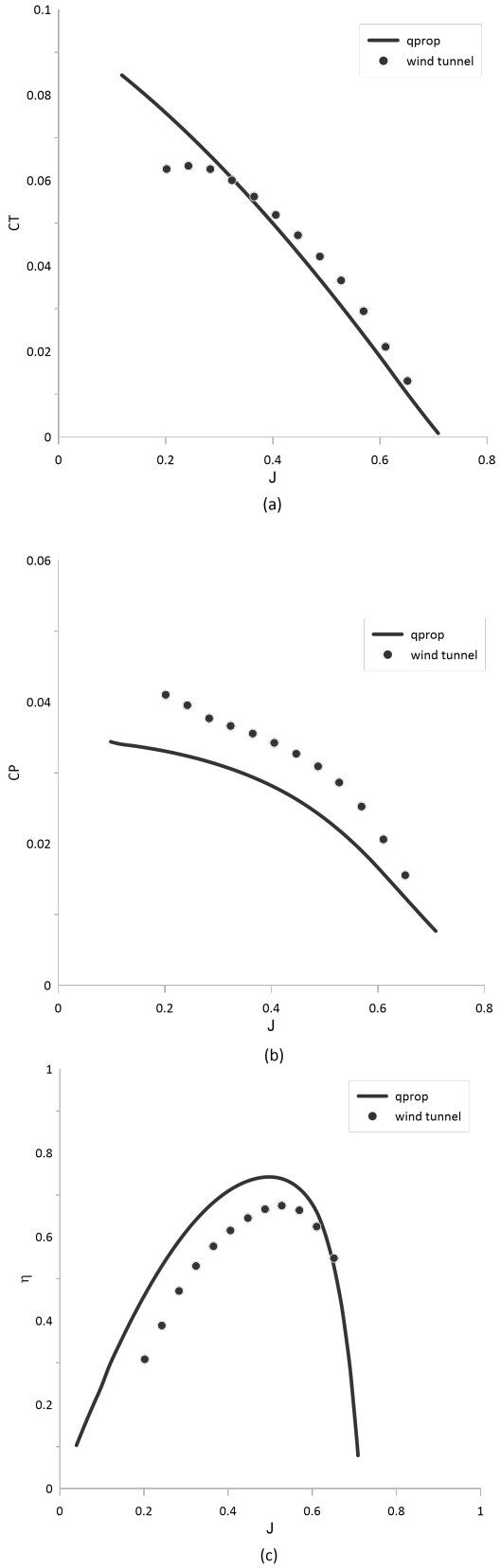

Figure 4.11: Thrust coefficient (a), power coefficient (b) and efficiency (c) vs advance ratio of $s9000_{14}$ propeller with no variation of its original pitch at 4000 rpm

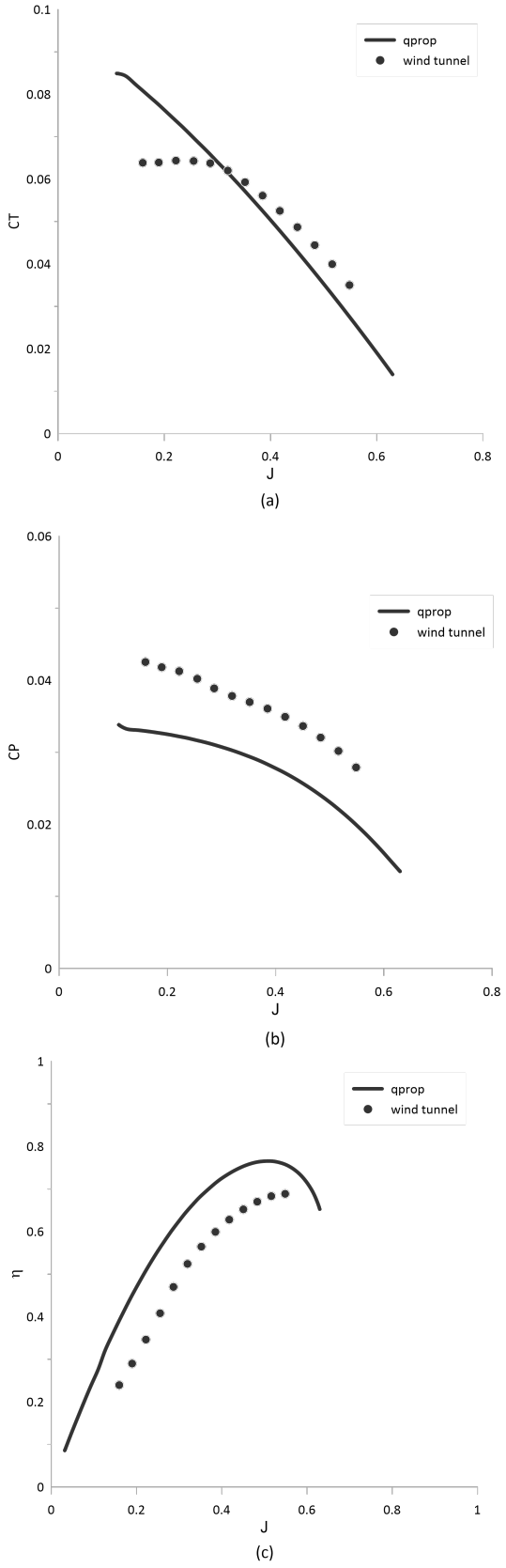

Figure 4.12: Thrust coefficient (a), power coefficient (b) and efficiency (c) vs advance ratio of $s9000_{14}$ propeller with no variation of its original pitch at 5000 rpm

4.4.3 High Pitch Setting: $\Delta\beta = +10^{o}$

In Figure 4.13, the performance results of $s9000_{14}$ used with a pitch incidence angle variation of +10 degrees considering its original design pitch obtained from QPROP and wind tunnel when it was tested at 3000 rpm are compared. The thrust coefficient (a), power coefficient (b) and propulsive efficiency (c) of the propeller as functions of advance ratio is represented.

As seen in Figure 4.13 the discrepancy between QPROP predictions and wind tunnel data results is even more accentuated for the coarse pitch condition ($\Delta\beta = +10$) where the maximum efficiency achieved in the wind tunnel experimental test at 3000 rpm is 14% lower than the value predicted with QPROP. The power coefficient calculated from the wind tunnel data is similar to the that obtained with QPROP for the range of values where a propeller with this pitch should be used but the thrust produced is significantly lower for the same range. It was only possible to obtain experimental results for 3000 rpm, since the propeller was presenting high vibration during the test for higher values of rotational speeds, possibly indicating a stalled blade condition, which would be unsurprising since the $S9000_{14}$ propeller was designed for maximum lift coefficient throughout the blade.

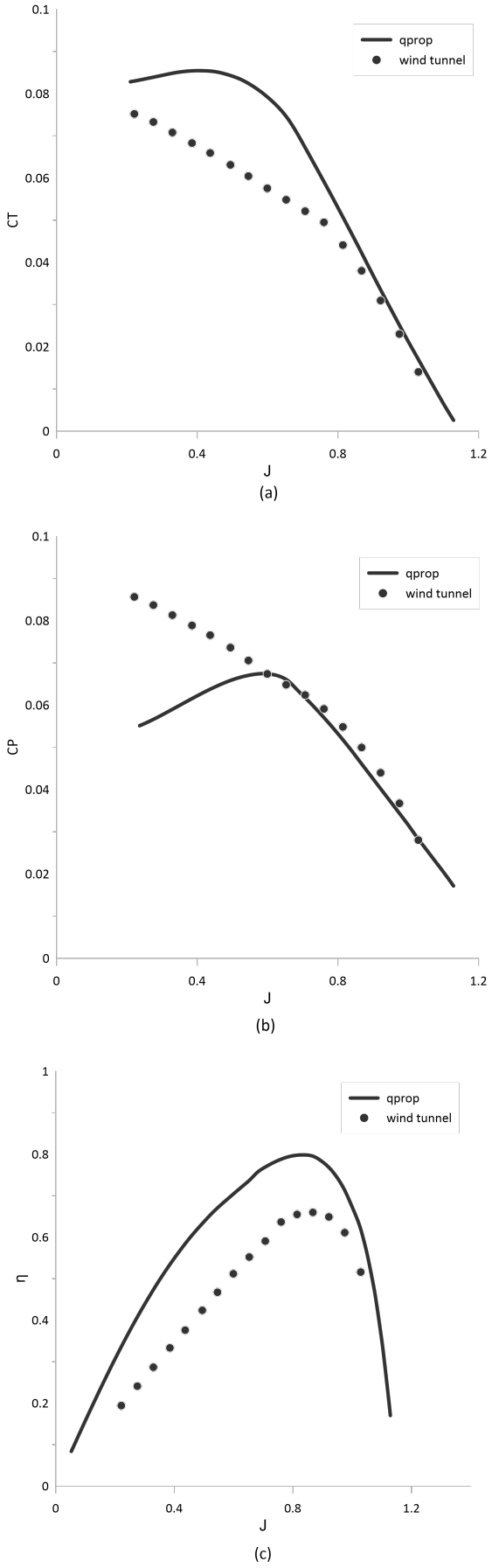

Figure 4.13: Thrust coefficient (a), power coefficient (b) and efficiency (c) vs advance ratio of $s9000_{14}$ propeller for $\Delta\beta$ variation of +10° at 3000 rpm

4.4.4 Maximum efficiency vs Pitch Setting

Since the goal was to develop a propeller with high efficiency values in a wide range of variable pitch operational conditions, in Figure 4.14 a comparison is made between the maximum efficiency values obtained in the three different pitch settings ($\Delta\beta$ -10, +0 and +10) that were tested in the wind tunnel with the equivalent propellers simulated with QPROP for rotational speed of 3000 (a), 4000 (b) and 5000 (c) rpm.

As seen in Figure 4.14 the difference between QPROP and wind tunnel results is evident as the propellers were tested at higher rotational speed. There are two main reasons that can explain the disparity:

1. $s9000_{14}$ propeller is characterized for presenting an airfoil with thin thickness. At 25% radius blade section, the chord near the root is approximately 46 mm but at 90% radius blade section the chord is near 11 mm. Noting that the propeller was 3D printed with PLA, some mechanical properties are not similar to a propeller manufactured with the traditional methods. Higher flexibility near the tip and lower near the root was visible in the 3D printed propeller. For the same value of rotational speed, in the coarse pitch operational condition the forces in the propeller are higher than in the low pitch operational condition, and it can justify that the discrepancy between numerical and experimental results becomes superior for coarser pitch operational conditions.

2. The other reason that can justify the difference between the results is the concept over which $s9000_{14}$ was designed. The propeller was designed to present a C_l value near the maximum of the airfoil until 80% of blade radius. Despite QPROP results predicting interesting performance values for variable pitch operational conditions, in the experimental test the propeller can be presenting stalled blade conditions at higher rotational speeds.

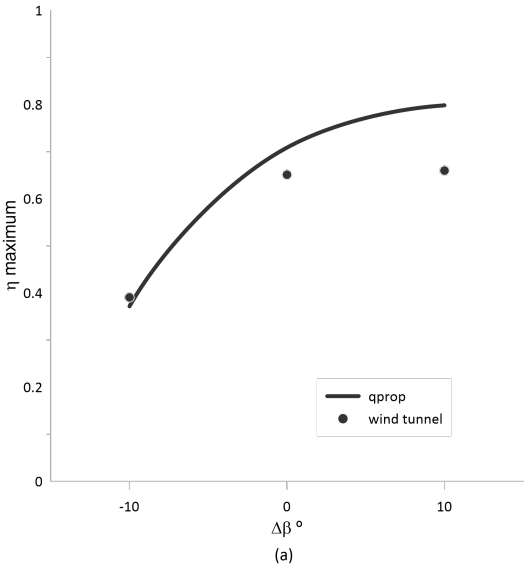

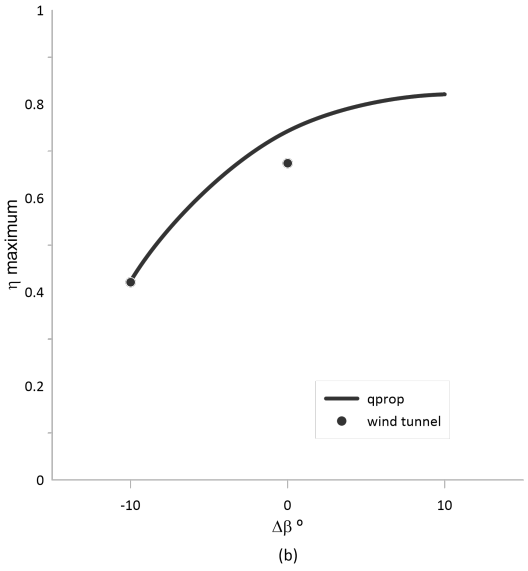

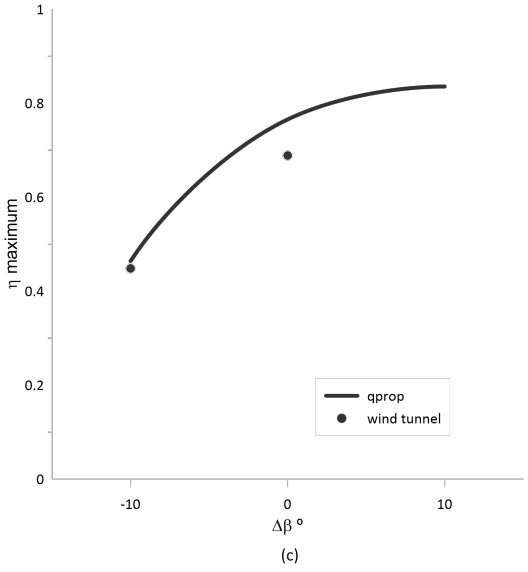

Figure 4.14: Maximum efficiency vs pitch incidence angle variation of $s9000_{14}$ at 3000 (a), 4000 (b) and 5000 (c) rpm

4.5 Numerical Study of the $S9000_{85}$ Propeller Blade Design

Mainly to certify if the second point previously presented for the disappointing performance of the $s9000_{14}$ is the reason for the difference between QPROP predictions and wind tunnel results, a new propeller ($s9000_{85}$) was 3D printed to be tested in the wind tunnel. This propeller was designed with a C_l distribution corresponding to the highest C_l/C_d value of the airfoil along the blade radius and a certain required shaft power for a specified airspeed and rotational speed in the design pitch condition as explained in Section 3.2.3.

The comparison of QPROP results of Aeronaut Camcarbon 15x8 and $s9000_{85}$ concerning their maximum efficiency as functions of pitch incidence angle variation at 6000 rpm can be seen in Figure 4.15 (the QPROP results of $s9000_{85}$ already include the adjustments applied to make the propeller 3D printed). The maximum efficiency of $s9000_{85}$ is higher than Aeronaut Camcarbon 15x8 for all the considered variable pitch operational conditions. Similarly to the previously $s9000_{14}$ design, larger differences for the low pitch condition and smaller differences for coarser pitch values.

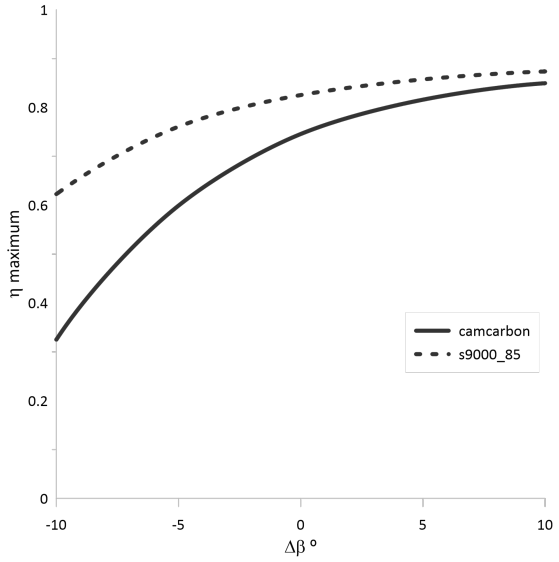

Figure 4.15: QPROP results of maximum efficiency vs pitch incidence angle variation of Aeronaut Camcarbon 15x8 and $s9000_{85}$ propellers at 6000rpm

In this case three propellers were not printed with different incidence angles but instead both blades were assembled to three different hubs designed to set the blade incidence angle variation of -10, 0 and 10 degrees.

4.5.1 Low Pitch Setting: $\Delta\beta = -10^{o}$

In Figures 4.16, 4.17 and 4.18 the performance results of $s9000_{85}$, used with a pitch incidence angle variation of -10 degrees considering its original design pitch, obtained from QPROP and wind tunnel when it was tested at three different rotational speeds are compared. In each figure the thrust coefficient (a), power coefficient (b) and propulsive efficiency (c) of the propeller as functions of advance ratio is represented.

As seen in Figures 4.16, 4.17 and 4.18, $s9000_{85}$ results obtained with QPROP and wind tunnel test data when the propeller was used in a low pitch condition ($\Delta\beta = -10^{o}$) present similar trends for the three values of tested rotational speeds. Both thrust coefficient and power coefficient values from the wind tunnel test data show a slightly lower offset value than predicted by QPROP, decreasing this gap as the rotational speed increases. The 3D printed propeller presents a very similar efficiency compared with QPROP prediction until its peak that is slightly lower than the simulation and occurs for a lower advance ratio. E.g. at 5000 rpm, maximum efficiency obtained in wind tunnel is about 2% lower than the predicted in QPROP and occurs for an advance ratio about 6.6% lower compared with the value from QPROP.

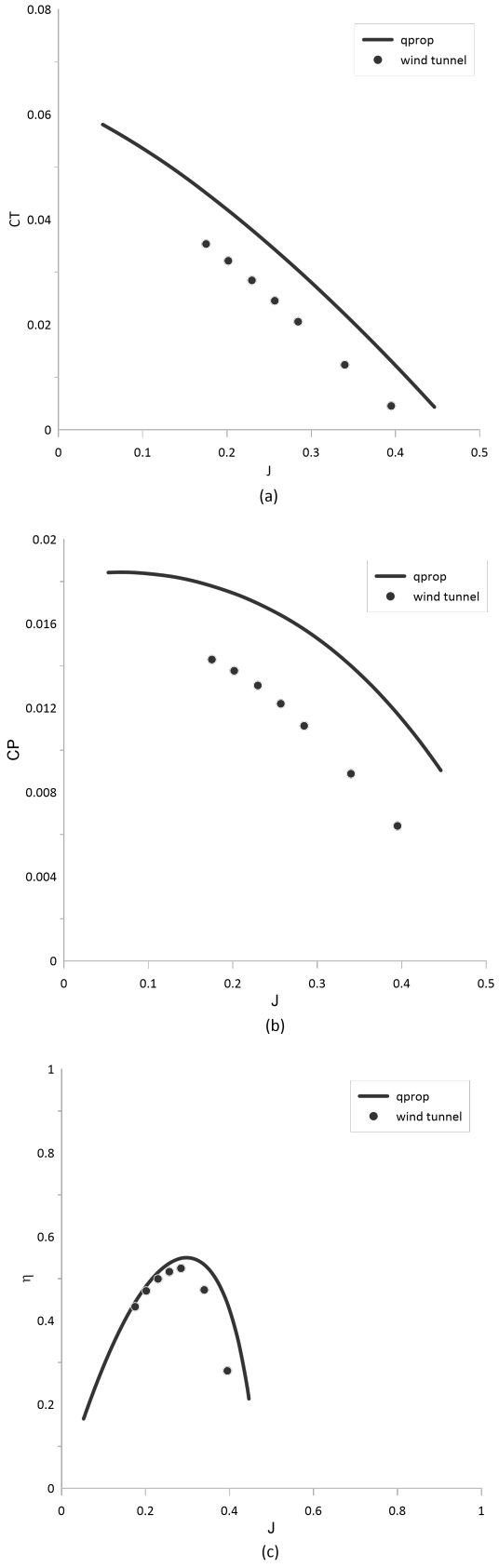

Figure 4.16: Thrust coefficient (a), power coefficient (b) and efficiency (c) vs advance ratio of $s9000_{85}$ propeller for $\Delta\beta$ variation of -10º at 3000 rpm

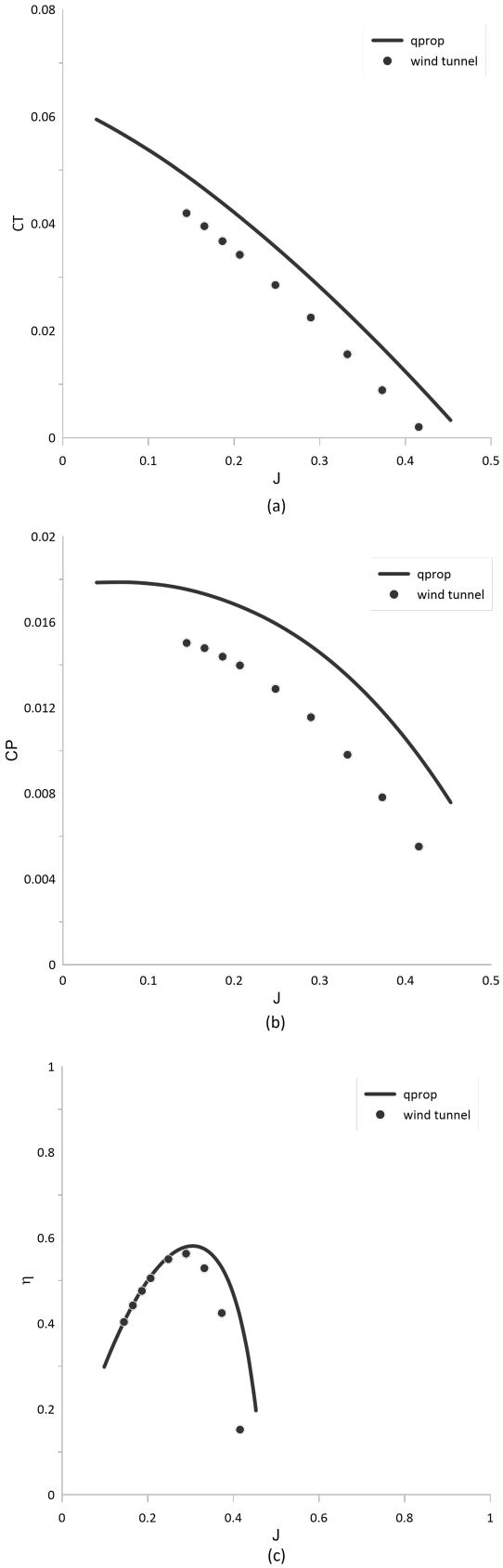

Figure 4.17: Thrust coefficient (a), power coefficient (b) and efficiency (c) vs advance ratio of $s9000_{85}$ propeller for $\Delta\beta$ variation of -10° at 4000 rpm

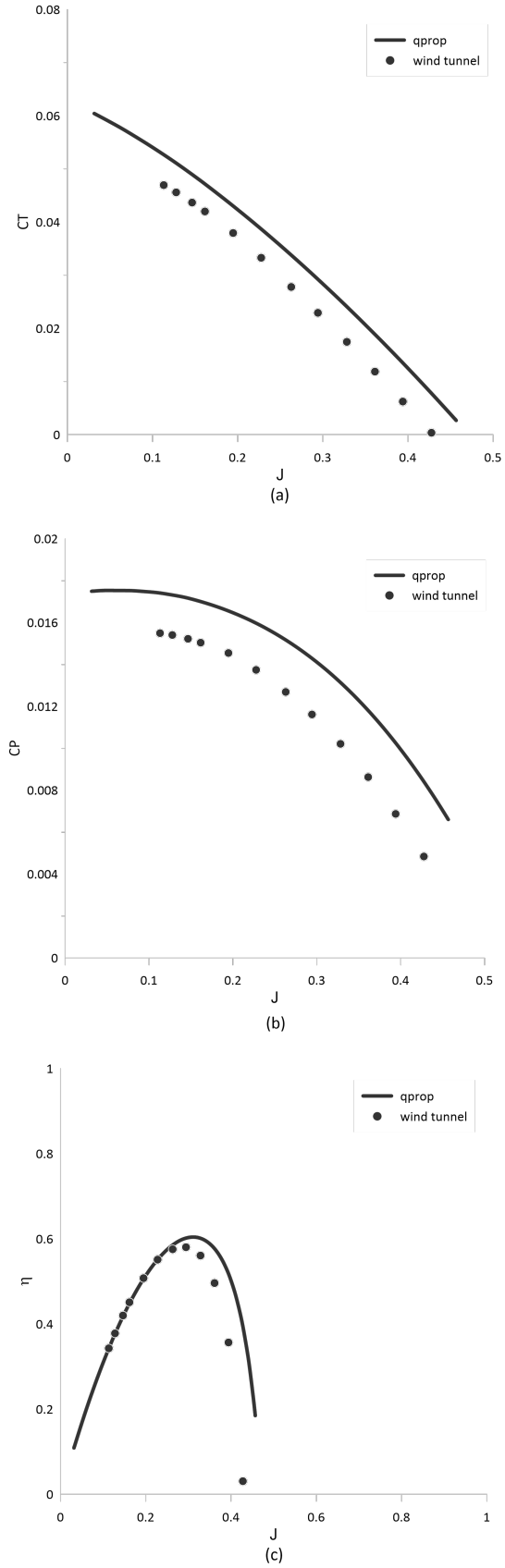

Figure 4.18: Thrust coefficient (a), power coefficient (b) and efficiency (c) vs advance ratio of $s9000_{85}$ propeller for $\Delta\beta$ variation of -10° at 5000 rpm

4.5.2 Design Pitch Setting: $\Delta\beta = +0^{o}$

In Figures 4.19, 4.20 and 4.21 the performance results of $s9000_{85}$, used with its designed pitch, obtained from QPROP and wind tunnel when it was tested at three different rotational speeds are compared. In each figure the thrust coefficient (a), power coefficient (b) and propulsive efficiency (c) of the propeller as functions of advance ratio is represented.

As seen in Figures 4.19 (c), 4.20 (c) and 4.21 (c) regarding the results of $s9000_{85}$ propeller tested for the three values of rotational speed with its design pitch, it is perceptible that the efficiency of 3D printed propeller is similar to the QPROP prediction until its peak that is slightly lower (about 3% in the absolute value for the three tested values of rotational speed) and occurs for a lower advance ratio (about 7% lower). This is the same trend observed in the low pitch condition. The thrust coefficient and power coefficient values from the simulation present a smooth function except for the lowest values of advance ratio, which is understandable since the propeller with the designed pitch (which is quite coarse) is not to be used in that range of smaller advance ratio values.

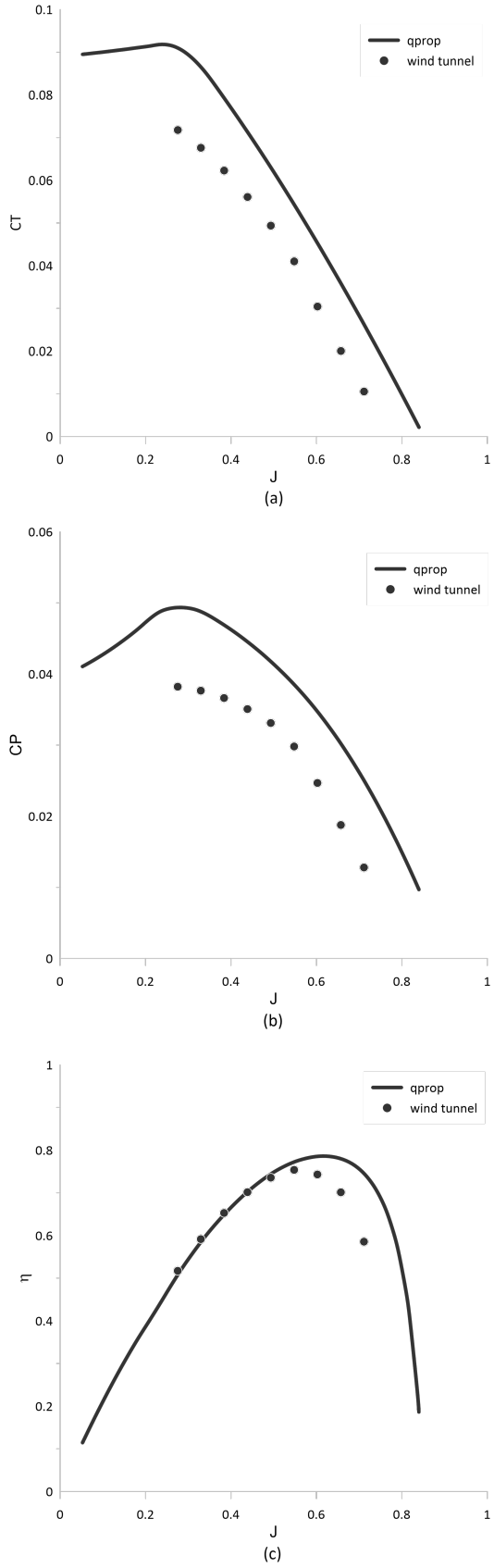

Figure 4.19: Thrust coefficient (a), power coefficient (b) and efficiency (c) vs advance ratio of $s9000_{85}$ propeller with no variation of its original pitch at 3000 rpm

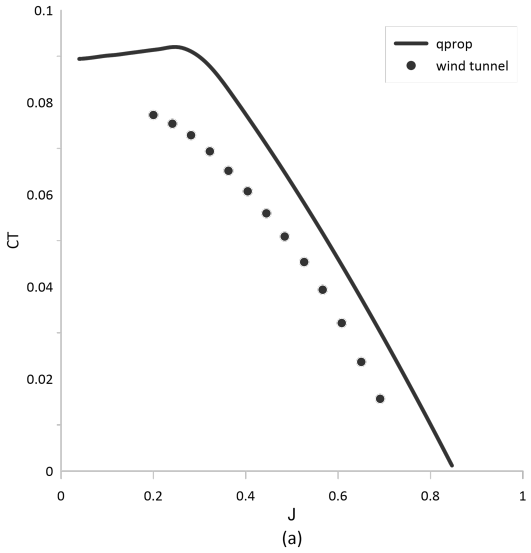

(a)

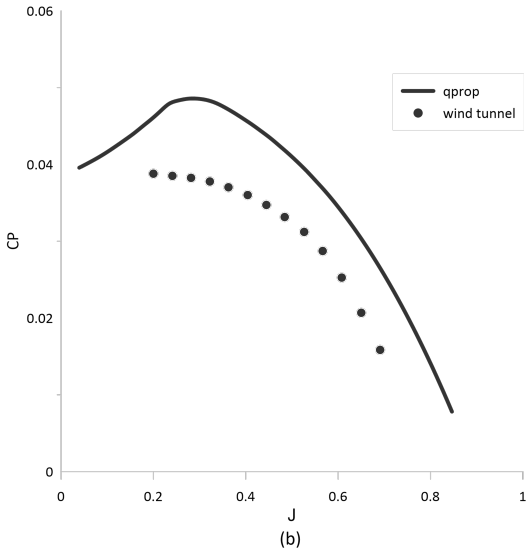

(b)

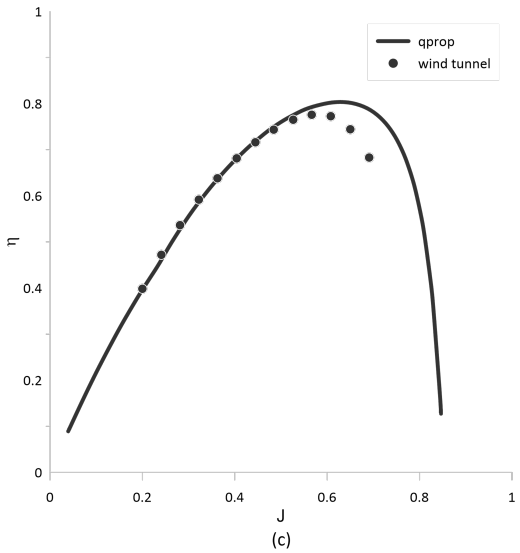

(c)

Figure 4.20: Thrust coefficient (a), power coefficient (b) and efficiency (c) vs advance ratio of $s9000_{85}$ propeller with no variation of its original pitch at 4000 rpm

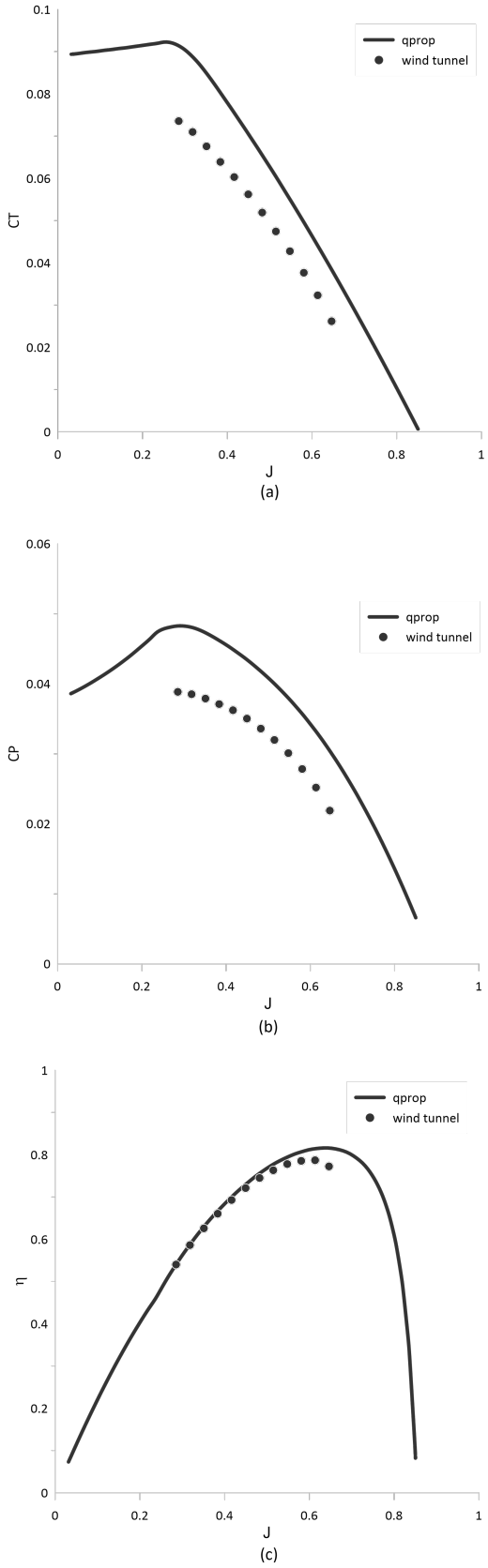

Figure 4.21: Thrust coefficient (a), power coefficient (b) and efficiency (c) vs advance ratio of $s9000_{85}$ propeller with no variation of its original pitch at 5000 rpm

4.5.3 High Pitch Setting: $\Delta\beta$ = $+10^{o}$

In Figures 4.22, 4.23 and 4.24 the performance results of $s9000_{85}$, used with a pitch incidence angle variation of +10 degrees considering its original design pitch, obtained from QPROP and wind tunnel when it was tested at three different rotational speeds are compared. In each figure the thrust coefficient (a), power coefficient (b) and propulsive efficiency (c) of the propeller as functions of advance ratio is represented.

As seen in Figures 4.22, 4.23 and 4.24, the simulation of $s9000_{85}$ considering β variation of +10 presents a smooth function for the thrust coefficient and power coefficient values, except for the lower advance ratio range, where the very coarse pitch blade is expected to be in a stalled. The corresponding values of C_t and C_p obtained from the wind tunnel data keep showing an offset to a lower value from the simulation values for the higher advance ratio values. In the 5000 rpm rotational speed case (Figure 4.24), the test in wind tunnel stopped when the propeller was reaching its maximum efficiency because of the wind tunnel maximum airspeed limitation. However, the maximum efficiency obtained from the tests at 3000 and 4000 rpm rotational speeds follow the same trend of this propeller, previously observed for the small and design pitch settings, occurring at a slightly lower value of advance ratio (about 4%) when compared with QPROP and 3% lower than the prediction.

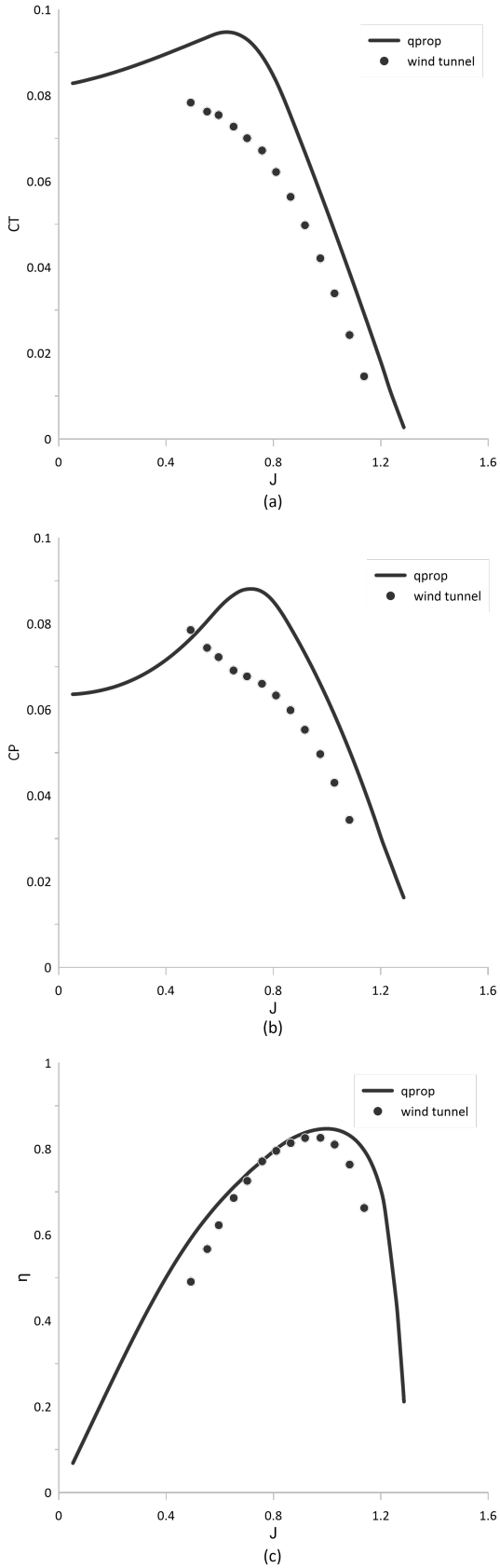

Figure 4.22: Thrust coefficient (a), power coefficient (b) and efficiency (c) vs advance ratio of $s9000_{85}$ propeller for $\Delta\beta$ variation of +10° at 3000 rpm

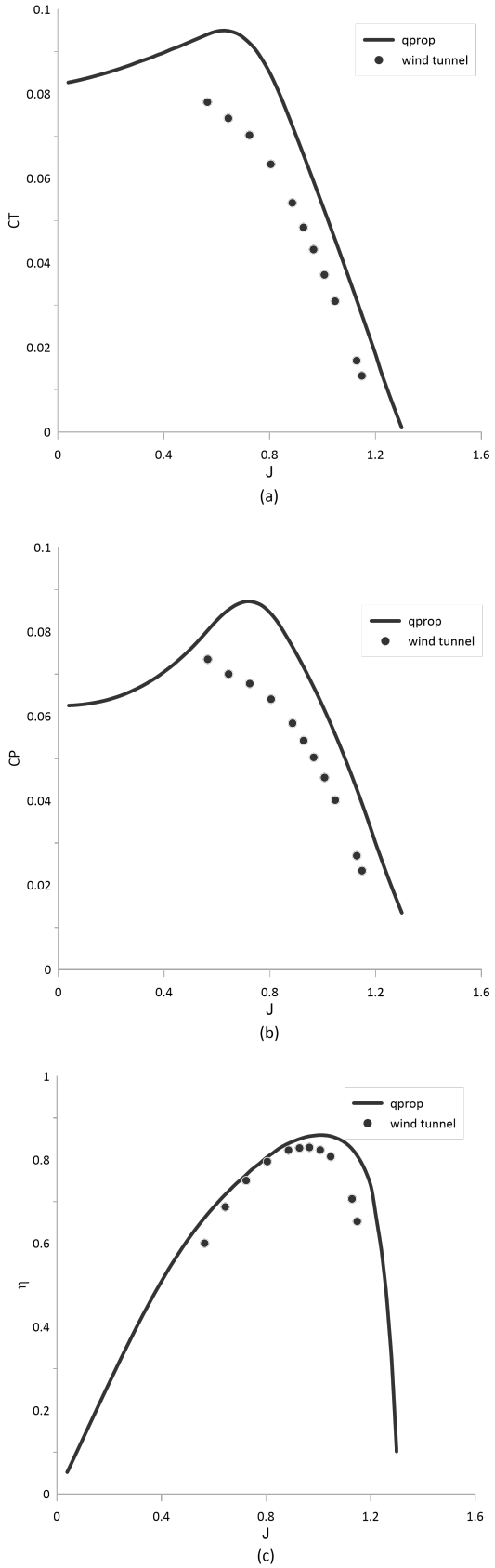

Figure 4.23: Thrust coefficient (a), power coefficient (b) and efficiency (c) vs advance ratio of $s9000_{85}$ propeller for $\Delta\beta$ variation of +10° at 4000 rpm

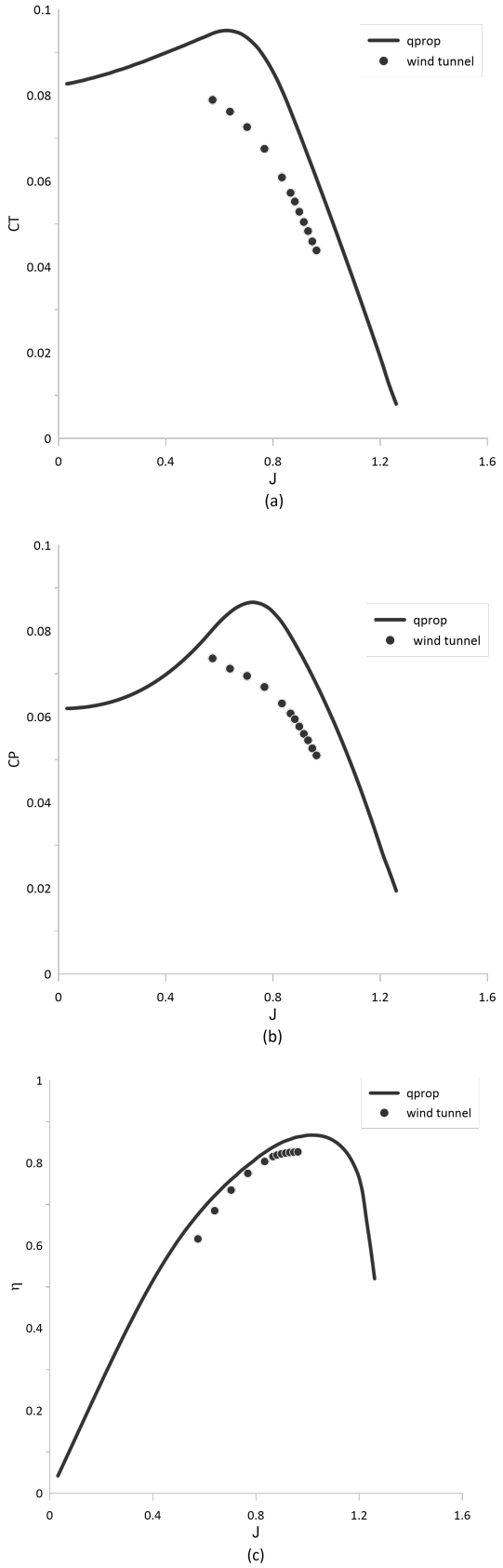

Figure 4.24: Thrust coefficient (a), power coefficient (b) and efficiency (c) vs advance ratio of $s9000_{85}$ propeller for $\Delta\beta$ variation of +10° at 5000 rpm

4.5.4 Maximum Efficiency vs Pitch Setting

In Figure 4.25 a comparison is made between the maximum efficiency values obtained in the three different pitch settings ($\Delta\beta$ -10, +0 and +10) that were tested in the wind tunnel with the equivalent propellers simulated with QPROP for rotational speed of 3000, 4000 and 5000 rpm.

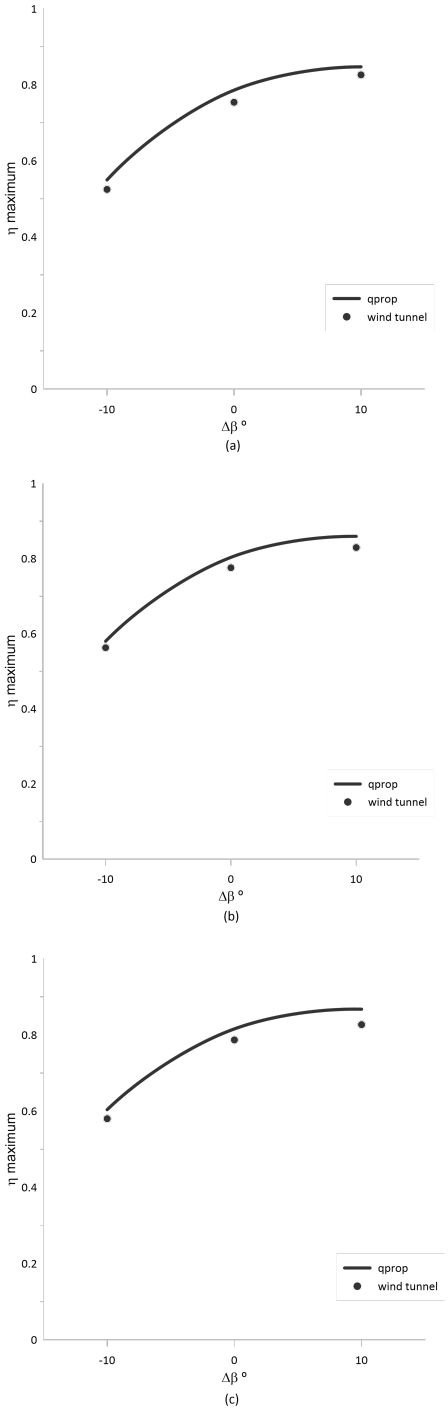

Figure 4.25: Maximum efficiency vs pitch incidence angle variation of $s9000_{85}$ at 3000 (a), 4000 (b) and 5000 (c) rpm

Observing the results from the following graphs (see Figure 4.25), the maximum efficiencies of the $s9000_{85}$ blade design obtained in wind tunnel in variable pitch operational conditions is slightly lower but close to the values predicted with QPROP simulations.

4.6 $S9000_{14}$ vs $S9000_{85}$ Propeller Blade Design

Comparing the results from $s9000_{14}$ and $s9000_{85}$ propellers, it appears that the reason why wind tunnel results of $s9000_{14}$ propeller do not accomplish the QPROP predictions is more related to the design concept of $s9000_{14}$ propeller blade than to the weaker mechanical properties associated to the 3D printing manufacturing process. The $s9000_{14}$ propeller blade was designed with close to maximum C_l values along the blade radius and it probably caused the printed propeller to face blade stalling conditions while it was tested in the wind tunnel. On the other hand, the values used in the QPROP input file to simulate airfoil characteristics generate functions that do not properly predict the stalling conditions of the airfoil and for that reason the results from the QPROP wrongly seemed to point to a good performance of the $s9000_{14}$ in variable pitch operational conditions.

Furthermore, comparing $s9000_{85}$ results with the propellers results presented in [29], there is a phenomenon that repeats in all the situations. The maximum efficiency of the propeller tested in the wind tunnel is always slightly lower and occurs for a slightly lower advance ratio value than predicted by the QPROP simulation. Additionally, thrust and power coefficients of the propellers tested in wind tunnel present lower values than those predicted by QPROP. These observable occurrences should be considered in the future development of propellers that make use of 3D printing manufacture process to analyze propeller prototypes.

Chapter 5

Conclusion

In this work different concepts were considered to design a propeller to be used in variable pitch operational conditions. One of those was chosen to be manufactured for a propeller prototype using a FDM 3D printer. The experimental results did not accomplish the numerical predictions of the propeller performance and the reasons behind the lower actual performance of the initially selected blade design concept were explained. Next, an alternative propeller blade design concept was considered, a new propeller was developed and this time the experimental results almost accomplished the numerical predictions.

Thus, the main objective of defining a suitable concept for the design of a propeller blade suitable for use with a variable pitch mechanism and validating the numerical prediction with experimental results obtained from a FDM 3D printed propeller prototype was achieved.

5.1 Future work

Following the work that has been done, some recommendations to improve propeller design to be used in a variable pitch mechanism are:

- Development or improvement of different airfoils to be used in different sections of the blade that can improve propeller performance and blade structure in variable pitch operational conditions.

- Implement Prandtl root correction in the blade design once it is not considered in the QMIL designing program while a recent study [26] has shown that it can improve the propeller performance.

Considering the wind tunnel results, the recommendation, as an attempt to get even more similar experimental results to those obtained from blades that use the traditional manufacturing techniques, is to use filaments reinforced with carbon fiber that provide more stiffness

in the blade structure, especially when a thin airfoil is used.

Bibliography

[1] J. Lu, B. Li, H. Li, and A. Ali, "Expansion of city scale, traffic modes, traffic congestion, and air pollution," *Cities*, vol. 108, 11 2020. 1

[2] P. Pradeep and P. Wei, "Energy-efficient arrival with RTA constraint for multirotor eVTOL in urban air mobility," vol. 16, no. 7, 2019, pp. 263–277. 1

[3] D. Finger, F. Götten, C. Braun, and C. Bil, "Initial sizing for a family of hybrid-electric VTOL general aviation aicraft," 09 2018. xi, 2

[4] C. J. Silva, W. Johnson, E. Solis, M. D. Patterson, and K. R. Antcliff, "VTOL urban air mobility concept vehicles for technology development," 2018. xi, 2

[5] A. Bacchini and E. Cestino, "Electric VTOL configurations comparison," *Aerospace*, vol. 6, p. 26, 02 2019. 2

[6] R. E. Froude, "On the part played in propulsion by differences of fluid pressure," *Trans. Inst. Naval Architects*, vol. 30, p. 390, 1889. 5

[7] W. J. M. Rankine, "On the mechanical principles of the action of propellers," *Transactions of the Institution of Naval Architects*, vol. 6, 1865. 5

[8] S. Drzewiecki, "Theory of air propellers and the method of their calculation/foreword by NB Delone," *Kiev: Publ. of RK Lubkovsky*, 1910. 6

[9] M. Drela, "QPROP formulation," *Massachusetts Inst. of Technology Aeronautics and Astronautics, Cambridge, MA*, 2006. xi, 7, 12

[10] H. Glauert, "Airplane propellers aerodynamic theory ed. WF Durand," 1935. 8

[11] L. Prandtl, "Gottinger klassiker der stromungsmechanik bd," 1919. 10

[12] I. Betz, "Screw propellers with minimum energy loss," *Göttingen Reports*, pp. 193–213, 1919. 12

[13] E. E. Larrabee, “Practical design of minimum induced loss propellers,” *SAE Transactions*, pp. 2053–2062, 1979. 12

[14] C. N. Adkins and R. H. Liebeck, “Design of optimum propellers,” *Journal of Propulsion and Power*, vol. 10, no. 5, pp. 676–682, 1994. 12

[15] M. Drela, “QPROP user guide,” *Massachusetts Inst. of Technology Aeronautics and Astronautics, Cambridge, MA*, 2007. 12, 19, 21

[16] ——, “QMIL user guide,” *Propeller Analysis and Design URL: http://web. mit. edu/drela/Public/web/qprop*, 2005. 12, 22

[17] B. Berman, “3-D printing: The new industrial revolution,” *Business horizons*, vol. 55, no. 2, pp. 155–162, 2012. 12

[18] G. D. Goh, S. Agarwala, G. Goh, V. Dikshit, S. L. Sing, and W. Y. Yeong, “Additive manufacturing in unmanned aerial vehicles (UAVs): Challenges and potential,” *Aerospace Science and Technology*, vol. 63, pp. 140–151, 2017. 12

[19] S. Easter, J. Turman, D. Sheffler, M. Balazs, and J. Rotner, “Using advanced manufacturing to produce unmanned aerial vehicles: a feasibility study,” in *Ground/Air Multisensor Interoperability, Integration, and Networking for Persistent ISR IV*, vol. 8742. International Society for Optics and Photonics, 2013, p. 874204. 13

[20] L. R. Toleos Jr, N. Luna, M. C. E. Manuel, J. M. R. Chua, E. M. A. Sangalang, and P. C. So, “Feasibility study for fused deposition modeling (FDM) 3D-printed propellers for unmanned aerial vehicles,” *International Journal of Mechanical Engineering and Robotics Research*, vol. 9, no. 4, pp. 548–558, 2020. 13, 14

[21] S. A. Khan, B. A. Siddiqui, and M. Fahad, “Evaluation of additive manufacturing techniques for fabrication of propellers for SUAVs,” in *2015 Fourth International Conference on Aerospace Science and Engineering (ICASE)*. IEEE, 2015, pp. 1–4. 13

[22] Y.-L. Yeh, “The standard strength test of 3D printing materials and its application for UAV propellers,” *Modern Physics Letters B*, vol. 34, no. 07n09, p. 2040017, 2020. 14

[23] M. Drela, “Propeller characterization for QPROP,” *URL: http://web. mit. edu/drela/Public/web/qprop/prop_measure. pdf,[cited 10 Feb 2011]*, 2005. xi, 15, 18, 20

[24] A. Rohatgi, “Webplotdigitizer. online,” 2018. 18

[25] [Online]. Available: http://www.xflr5.tech/xflr5.htm 20

[26] H. Rocha, P. Alves, A. Rodrigues, and M. Silvestre, in *Proceedings of AeroBest 2021-International Conference on Multidisciplinary Design Optimization of Aerospace Systems (p.305)*, Lisboa, Portugal, 21-23 July 2021. 22, 71

[27] A. H. Bowers, O. J. Murillo, R. R. Jensen, B. Eslinger, and C. Gelzer, “On wings of the minimum induced drag: Spanload implications for aircraft and birds,” Tech. Rep., 2016. 22

[28] A. H. Bowers, “Prandtl wing minimum drag update,” 2018. [Online]. Available: https://www.youtube.com/watch?v=bCwtcDNB15E 22

[29] P. Alves, M. Silvestre, and A. Rodrigues, “Assessment of low cost FDM 3D printing in low Reynolds number propeller prototyping,” in *AIAA Propulsion and Energy 2021 Forum*. [Online]. Available: https://arc.aiaa.org/doi/abs/10.2514/6.2021-3226 xi, 31, 32, 69

[30] P. J. F. Alves, “Low Reynolds number propeller performance measurement in wind tunnel test rig,” Ph.D. dissertation, 2014. xi, 33, 34